

AD-A232 424

802-767-6962

2

REPORT DOCUMENTATION PAGE

1a. REPORT SECURITY CLASSIFICATION Unclassified		1b. RESTRICTIVE MARKINGS	
2a. SECURITY CLASSIFICATION AUTHORITY		3. DISTRIBUTION / AVAILABILITY OF REPORT Approved for public release, Distribution unlimited	
2b. DECLASSIFICATION / DOWNGRADING SCHEDULE MAR 11 1991		5. MONITORING ORGANIZATION REPORT NUMBER(S) AFOSR-TR- 91 0181	
4. PERFORMING ORGANIZATION REPORT NUMBER MIT-CE-R-90-22		6a. NAME OF PERFORMING ORGANIZATION Massachusetts Institute of Tech. Dept. of Civil Engineering	
6b. OFFICE SYMBOL (If applicable)		7a. NAME OF MONITORING ORGANIZATION U.S. Air Force Office of Scientific Research	
6c. ADDRESS (City, State, and ZIP Code) 77 Massachusetts Avenue Cambridge, Massachusetts 02139		7b. ADDRESS (City, State, and ZIP Code) Bid 410 Bolling Air Force Base Washington D.C. 20332-6445	
8a. NAME OF FUNDING / SPONSORING ORGANIZATION AFOSR and AFESC		8b. OFFICE SYMBOL (If applicable) NA	
8c. ADDRESS (City, State, and ZIP Code) AFOSR - Bolling AFB, Washington D.C. 20332-6448 AFESC - Tallahassee AFB, Florida 32404-6061		9. PROCUREMENT INSTRUMENT IDENTIFICATION NUMBER AFOSR-87-0260	
10. SOURCE OF FUNDING NUMBERS			
PROGRAM ELEMENT NO 61102F	PROJECT NO. 2302	TASK NO. C2	WORK UNIT ACCESSION NO.
11. TITLE (Include Security Classification) Stochastic and Centrifuge Modelling of Jointed Rock - Executive Summary			
12. PERSONAL AUTHOR(S) Herbert H. Einstein, Victor Li, Robert V. Whitman, Daniele Veneziano Olivia Reyes, Gerald Iglesia, Jun-Suk Lee			
13a. TYPE OF REPORT Final	13b. TIME COVERED FROM 6/87 TO 5/90	14. DATE OF REPORT (Year, Month, Day) 1990, August, 31	15. PAGE COUNT 95
16. SUPPLEMENTARY NOTATION			
17. COSATI CODES		18. SUBJECT TERMS (Continue on reverse if necessary and identify by block number)	
FIELD	GROUP	SUB-GROUP	
		Jointed (Fractured) Rock, Stochastic Modelling, Fracture Geometry	
19. ABSTRACT (Continue on reverse if necessary and identify by block number)			
<p>This Executive Summary presents the major results in the three research areas: Fracturing of Jointed Rock, Centrifuge Testing of Jointed Rock and Stochastic Modelling of Jointed Rock. A separate volume of this final report is devoted to each of these research areas, namely, Volume I: "Fracturing of Fractured Rock", Volume II: "Centrifuge Modelling of Jointed Rock", Volume III, "Stochastic and Topological Fracture Geometry Model".</p> <p>(Continued on next page.)</p>			
20. DISTRIBUTION / AVAILABILITY OF ABSTRACT <input type="checkbox"/> UNCLASSIFIED/UNLIMITED <input type="checkbox"/> SAME AS RPT <input type="checkbox"/> DTIC USERS		21. ABSTRACT SECURITY CLASSIFICATION UNCLASSIFIED	
22a. NAME OF RESPONSIBLE INDIVIDUAL DR S WU		22b. TELEPHONE (Include Area Code) 802-767-6962	22c. OFFICE SYMBOL NA

Block 19 - continued

Research in area I resulted in the discovery of a new fracture coalescence mode and in an analytical model for this. Research in area II led to a more accurate recognition of arching and to an appropriate predictive model; it also showed to which extent centrifuge modelling can be applied to discontinua. Finally, research in area III led to a stochastic fracture geometry model which can accurately represent actual fracture trace geometries and the sequential genesis of fractures; this model was incorporated in a new topological slope stability model.

MIT CE R-90-22

STOCHASTIC AND  
CENTRIFUGE  
MODELLING OF JOINTED  
ROCK

**Executive Summary**

Grant No. AFOSR-87-0260

Final Report 1990

Prepared by

H. H. Einstein

and

V. Li

R. V. Whitman

D. Veneziano

O. Reyes

G. Iglesia

J. S. Lee

Sponsored by

U.S. Air Force  
Air Force Office of Scientific Research  
Bolling Air Force Base  
Air Force Engineering Services Center  
Tyndall Air Force Base

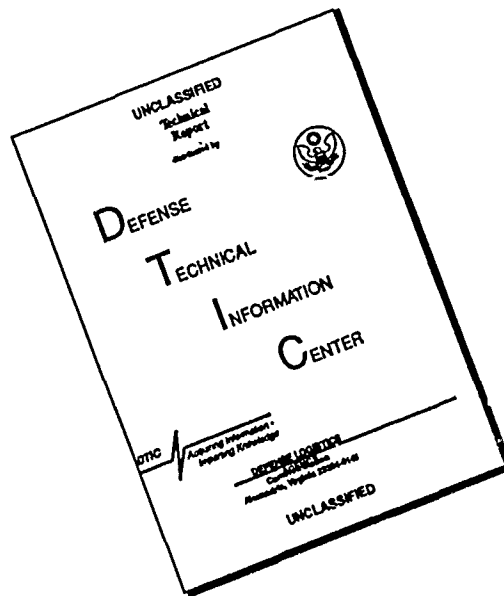
December 1990

MIT

DEPARTMENT  
OF  
CIVIL  
ENGINEERING

SCHOOL OF ENGINEERING  
MASSACHUSETTS INSTITUTE OF TECHNOLOGY  
Cambridge, Massachusetts 02139

# DISCLAIMER NOTICE



THIS DOCUMENT IS BEST QUALITY AVAILABLE. THE COPY FURNISHED TO DTIC CONTAINED A SIGNIFICANT NUMBER OF PAGES WHICH DO NOT REPRODUCE LEGIBLY.



## 1. Introduction

The research on Stochastic and Centrifuge Modelling of Jointed Rock has been performed during the years 1987 to 1990 under sponsorship of the U.S. Air Force Office of Scientific Research and the U.S. Air Force Engineering Services Center. It represents a logical continuation of preceding work by the PI's on geometric and mechanical modelling of jointed rock and centrifuge studies on granular material.

The research was subdivided into three major areas, namely:

Fracturing of Jointed\* Rock  
Centrifuge Modelling of Jointed Rock  
Stochastic Modelling of Jointed Rock

which are parts of an entity, the behavior of a jointed mass. Stochastic modelling of jointed rock is necessary to represent the geometry of rock masses. Fracturing of jointed rock is a possible mechanism underlying rock mass behavior in which a jointed (or discontinuous mass deforms and eventually fails as new fractures connect existing ones. The other major mechanism of rock mass failure is relative sliding of blocks bounded by existing joints or by existing joints and newly created fractures; this can be physically modelled in the centrifuge under realistic stress conditions.

The combination of geometric and mechanical modelling of a jointed mass seems to be an obvious approach. Previous work of our group and others in the area suffer, however, from several inadequacies or lack of knowledge. Stochastic and other geometric models which existed prior to the research reported here were usually not capable of representing the actual geometry of a rock mass even if the information mass was carefully sampled from it.

---

\* Throughout this report the terms "joint" and "fracture" will be used interchangeably.

The occurrence of new fractures in a discontinuum was not well understood, in particular, only limited experimental observations and analytical models existed. While the basic understanding of movement of rigid blocks bounded by discontinuities exists, analytical modelling usually relies on limit equilibrium approaches which neglect the real stress distribution. Physical experiments were not adequate to represent geostatic stress distribution, or if they were, such as centrifuge experiments, doubts existed as to the applicability of centrifuge testing to discontinua.

The research described in this report made significant contributions in the three problem areas, through the development of a stochastic model which can represent real joint geometry, through experimentation and analytical modelling of fracturing between existing joints, and through centrifuge experimentation which establishes the limitations of this method with regard to testing of discontinua. The research went beyond these contributions in that the stochastic model was combined with a topological model for slope stability, in that the fracture coalescence work provided general insight into fracturing of discontinuous brittle materials, and in that the centrifuge investigation led to a complete understanding and analytical modelling for arching of granular continua and of discontinua. As we will show in the conclusions, this research not only led to major advances in the fundamental understanding of geometric and mechanical behavior of rock masses, but it also advanced fundamental knowledge on brittle discontinua in general, and it provided results which have substantial practical significance.

The report is subdivided into three parts corresponding to the three research areas:

Part I: Fracturing of Fractured Rock

Part II: Centrifuge Modelling of Jointed Rock

Part III: Stochastic and Topological Fracture Geometry Model

each of which is contained in a separate volume. In the following lines we will summarize in the same sequence the major aspects of the work and the most important results.

## 2. Fracturing of Fractured Rock

### 2.1 Problem Statements and Schedule of Research

Fracturing of 'intact' (or otherwise expressed, continuous) brittle material has received attention over many years both in theoretical and experimental research. Much less work has been performed on fracturing of fractured rock, i.e. of the rock mass containing discontinuities. This is so inspite of the fact that many natural and engineering problems associated with rock masses involve the propagation of fractures between existing discontinuities such as faults, joints, foliation surfaces and bedding planes. Examples where this process is important, are natural phenomena such as joint genesis, faulting and landslides, and engineered structures such as slopes and tunnels. Although usually on a smaller scale, similar fracturing between existing fractures or cracks occurs in other materials, notably, concrete but also in polymers and ice. What is discussed here under the catchphrase "fracturing of fractured rock" includes thus all problems where a 'new' fracture emanates from an existing discontinuity and propagates to connect with another discontinuity.

During the first year of research (see Annual Report 1987/88) the research was divided into two major areas, namely, the development of a numerical model for tension softening materials and the preparation and performance of initial tests on fracturing model materials with pre-existing fractures. The numerical model for a tension softening material was not only developed but also validated. All this is reported in addition to the Annual Report 87/88, in the M.S. thesis, "Numerical Modelling of Fracture Propagation in Tension Softening Materials"\* , by O.M. Reyes and a paper, "Numerical Modelling of Fracture Propagation in Tension Softening Materials", by Reyes, Li, Einstein which is ready to be submitted to a professional journal. In the experimental work during the first year, we selected the model materials, a gypsum and an epoxy resin. The material properties were determined, and, most

---

\*For literature references, see Appendix A.

importantly, a variety of procedures for molding of pre-fractured model specimens were investigated. Initial tests were run which revealed different types of cracks emanating from the pre-existing fractures or flaws.

These initial tests and follow-up tests during the second year (see Annual Report 1988/89) indicated the importance of procedures which would allow us to observe the crack propagation in detail. Therefore, a substantial effort was developed to the study of different observation methods including high speed film and videotaping. The required resolutions led us to select a procedure in which observation through a microscope ( $\sim 20 \times$  magnification) is combined with the possibility to taking photographs. Test series conducted with this equipment then revealed the surprising fact that, in contrast to earlier analytical studies and experiments, coalescence of pre-existing non-overlapping fractures in gypsum occurred through so called secondary cracks which develop after the well known wing crack (Fig. 2.1). Simultaneously, we investigated possible analytical and numerical approaches to model this behavior which led us to the conclusion that we had to develop our own model.

The detailed test series in which we observed fracture coalescence and the development of the associated predictive model were the subject of the third year of research and are described in Volume I of this report series as well as in the following summary.

## 2.2 Coalescence Experiments

### 2.2.1 Procedures

Uniaxial compression tests were run on prismatic specimens as shown in Fig. 2.2. The material used is a hydrated gypsum made from a mixture of gypsum (Hydrocal B-11), celite (diatomaceous earth) and water at ratios water:gypsum = 0.4 and water: celite = 35. This gypsum is essentially the same material as that used in preceding MIT model rock experiments because it is well suited for

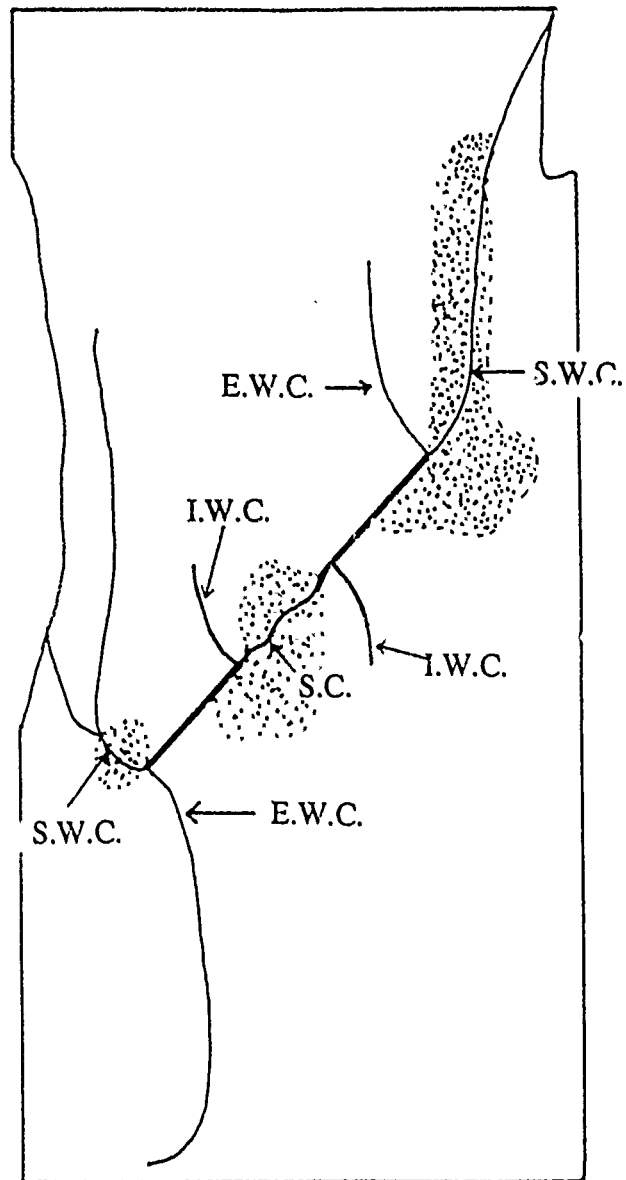


Figure 2.1. Observed Crack Types: E.W.C.=External Wing Crack; I.W.C.=Internal Wing Crack; S.C.=Secondary Coalescing Crack (Called "Secondary Crack" in the text); S.W.C.=Secondary Wing Crack.

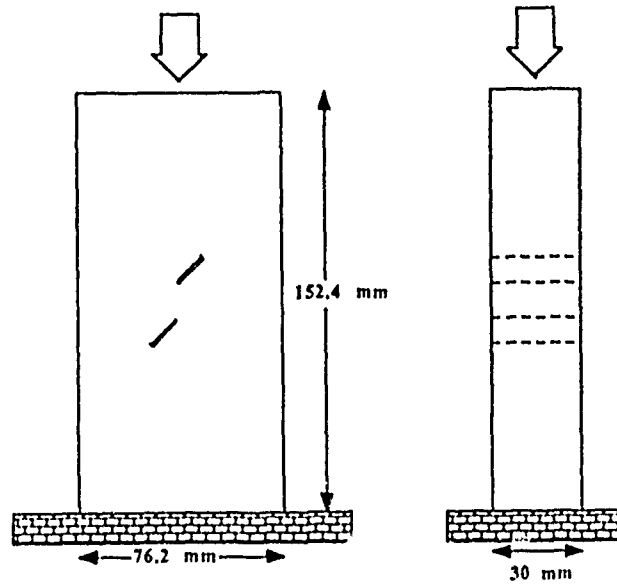


Figure 2.2. Geometry of Fractured Specimens

The geometry of the pre-existing fractures was chosen as follows:

- Each block had two 12.7 mm long pre-existing fractures separated by a rock bridge which was also 12.7 mm in length. The fractures had a finite open width of ~0.25 mm and stayed open during compression testing. This had the advantage of eliminating friction between fracture surfaces which is difficult to quantify.
- The fractures were inclined at 30°, 45° and 60° to the horizontal with both fractures always at the same inclination in a particular specimen.
- The rock bridge inclination was the other main variable in this study (see Figure 2.3). The fracture geometries can be characterized as either overlapping or non-overlapping, depending on the inclination of the rock bridge with respect to the direction of the applied uniaxial compressive load (see Figure 2.4)

As mentioned before, we used a microscope (20×) to monitor crack growth. Since the field of view through the microscope is rather small, step loading was also adopted in order to allow enough time for the entire surface to be scanned after each load increment. This was possible because crack propagation in compression is a stable process prior to strength failure, and no creep could take place during the short time intervals that the load was held constant at each step. Steps were displacement controlled with displacements of approximately 0.005 to 0.015 mm per step.

### 2.2.2 Observations and Results of Coalescence Experiments

For all fracture geometries, wing cracks at the outer and inner fracture tips appeared first. This was followed by fracture coalescence through wing crack growth for overlapping fractures, and coalescence through secondary crack growth for non-overlapping fractures. Fig. 2.5 shows coalescence between overlapping 30°-135° (30° fracture inclination-135° rock bridge inclination) fractures; in this case, the lower internal wing crack propagated towards the tip of the upper fracture. (The term "internal" and "external" refer to

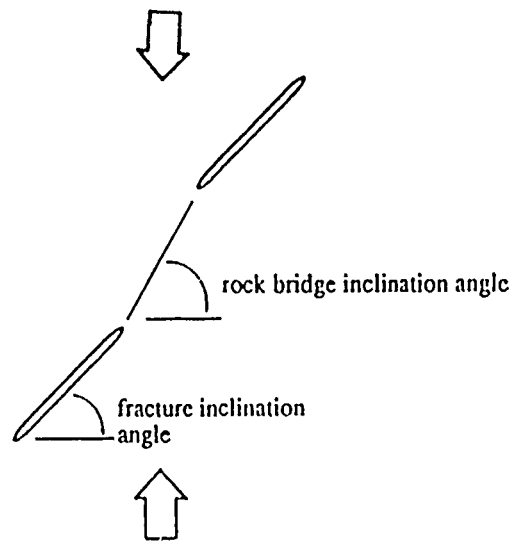


Figure 2.3. Fracture and Rock Bridge Geometries

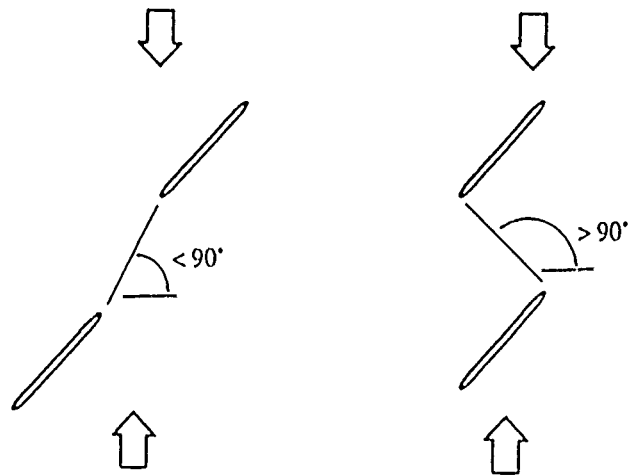


Figure 2.4. Non-overlapping (left) and Overlapping (right) Fractures

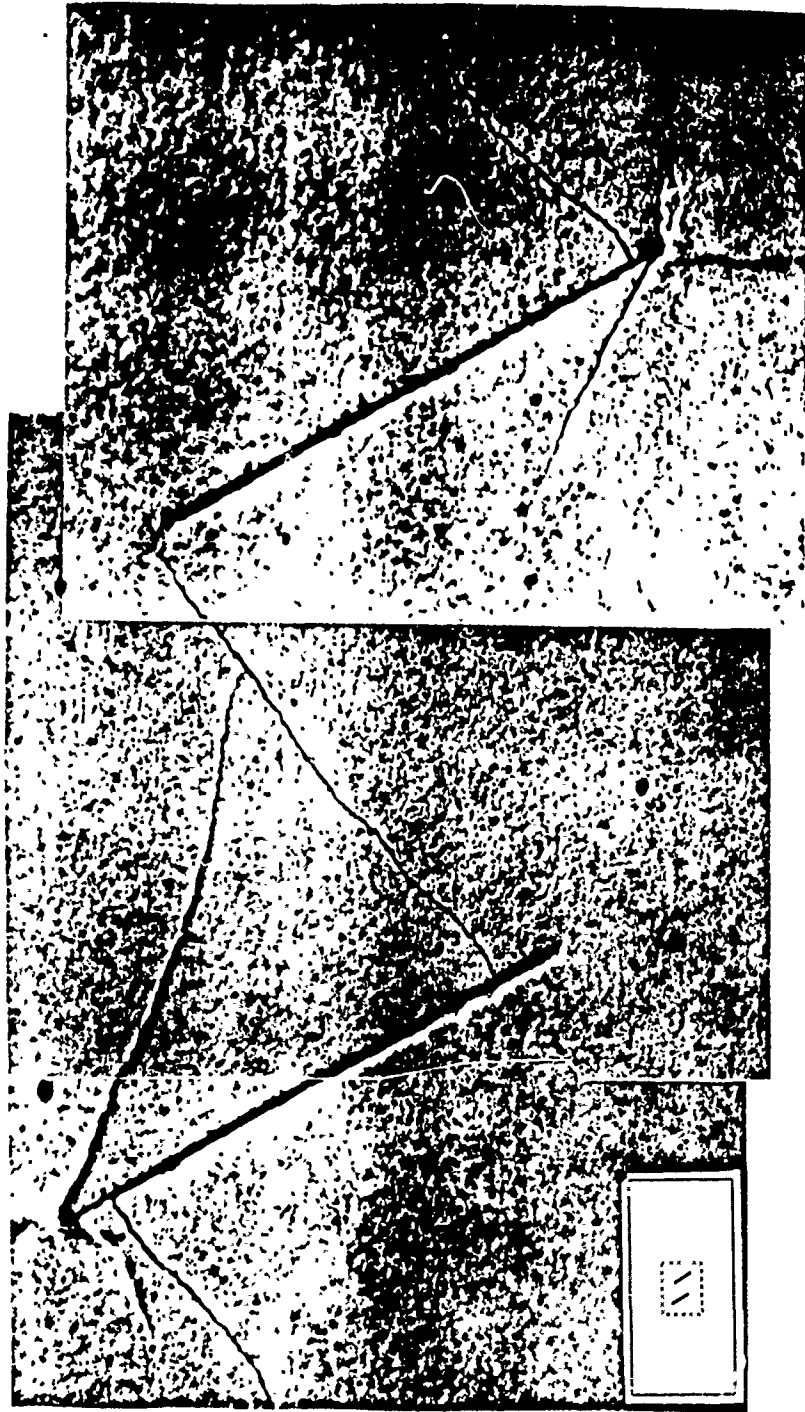


Figure 2.5. Fracture Coalescence for Overlapping Pre-existing Fractures

location of the wing crack with respect to the pair of existing fractures, see Fig. 2.1) Figs. 2.6-2.9 show the load-displacement curve (Fig. 2.6) and photographs (Fig. 2.7-2.9) of the fracture coalescence process for the non-overlapping  $30^{\circ}$ - $45^{\circ}$  fractures ( $30^{\circ}$  fracture inclination -  $45^{\circ}$  rock bridge inclination). For this geometry, wing cracks first appeared at an applied load of 25 kN (equivalent to 11 MPa assuming uniform distribution on the loading surface). Fig. 2.7, a photograph taken at a load of 47 kN (21 MPa), shows these wing cracks as well as some spalling near the fracture tips. At an applied load of 54 kN (24 MPa), coalescence suddenly occurred (Fig. 2.8); this happened so rapidly that we were not able to establish if the propagation direction was from the rock bridge center toward the fracture tips or vice versa. Fig. 2.9 is an expanded view of the  $30^{\circ}$ - $45^{\circ}$  fractures after coalescence. Note that the internal wing cracks are closed while the external ones are open, perhaps indicating that the stresses which were keeping the internal wing cracks open were relieved by the formation of the coalescence crack.

The coalescence process observed with  $30^{\circ}$ - $45^{\circ}$  pre-existing fractures is essentially the same for all other non-overlapping fractures, i.e., a secondary crack grows within the rock bridge and connects the inner fracture tips. Differences exist with regard to: (1) measured loads at which coalescence occurred and (2) surface characteristics of coalescence cracks as will be discussed below.

In addition to observing crack geometry and sequence, we also studied the details of the crack surfaces. This fractographic study is described in detail in Volume I of this report series. It showed us that coalescence cracks may involve a complex interaction of tensile and shear fractures as well as post fracture shearing.

In general, for the same fracture inclination angles, the coalescence loads were lower for non-overlapping compared to overlapping fracture geometries. Non-overlapping fractures are thus more critical at least in unconfined compression. Furthermore, secondary crack growth associated with the coalescence of non-overlapping fractures cannot be explained by existing fracture mechanics theories. We, therefore, concentrated on non-overlapping fractures in our predictive model as will be discussed below and in

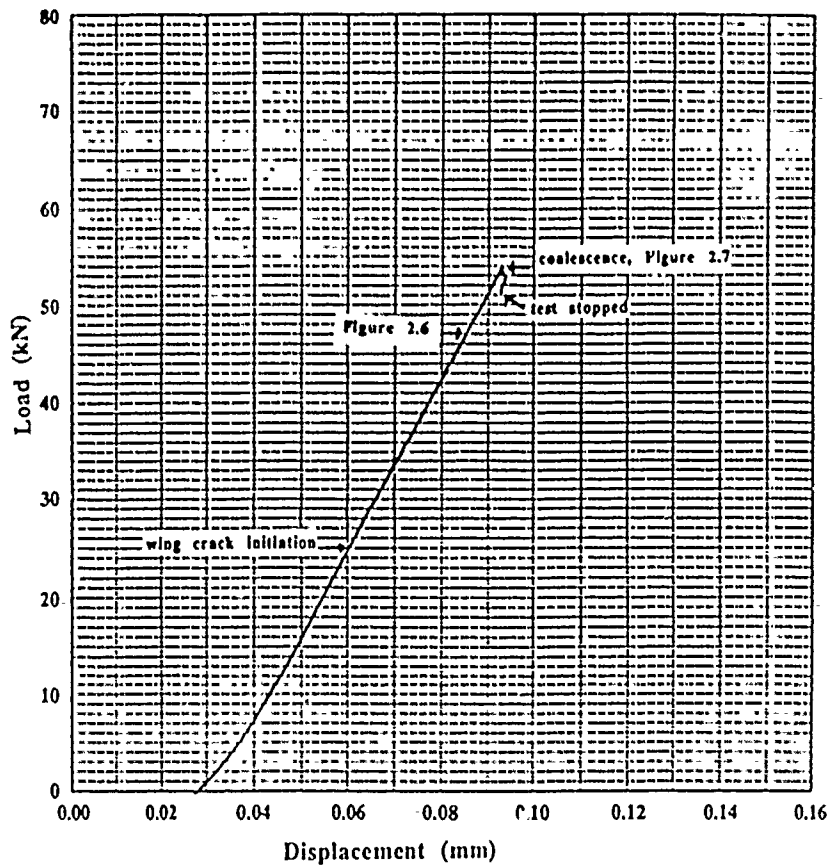


Figure 2.6. Load-Displacement Curve for Uniaxial Compression Test on 30°-45° specimen (see also Figs. 2.6 and 2.7)



Figure 2.7. Uniaxial Compression Test on  $30^{\circ}$ - $45^{\circ}$  Specimen, Load Level = 47 kN, Wing Cracks and Some Spalling Can Be Observed

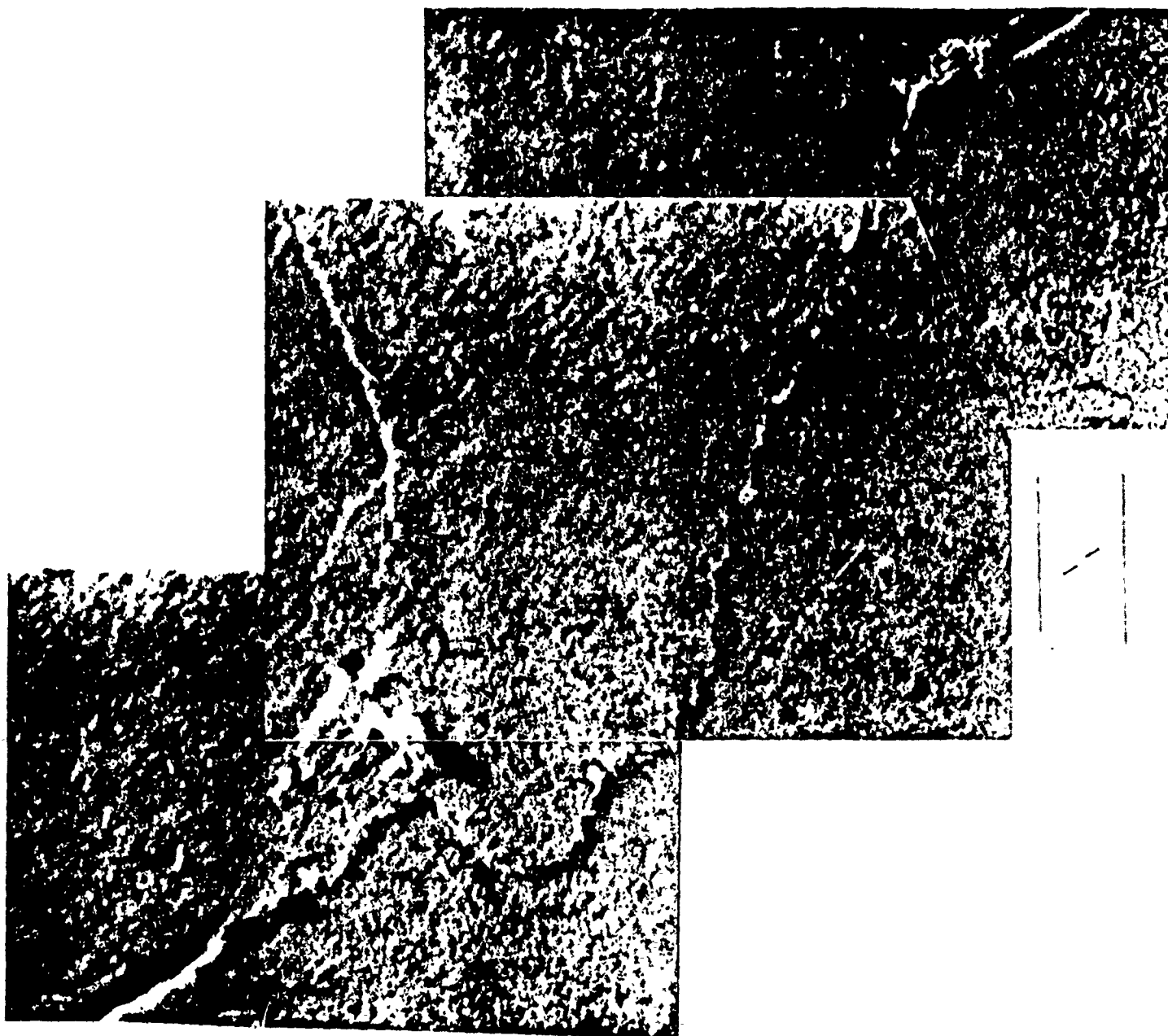


Figure 2.8. Uniaxial Compression Test on  $30^{\circ}$ - $45^{\circ}$  Specimen, Load Level = 54 kN, Secondary Crack has Propagated

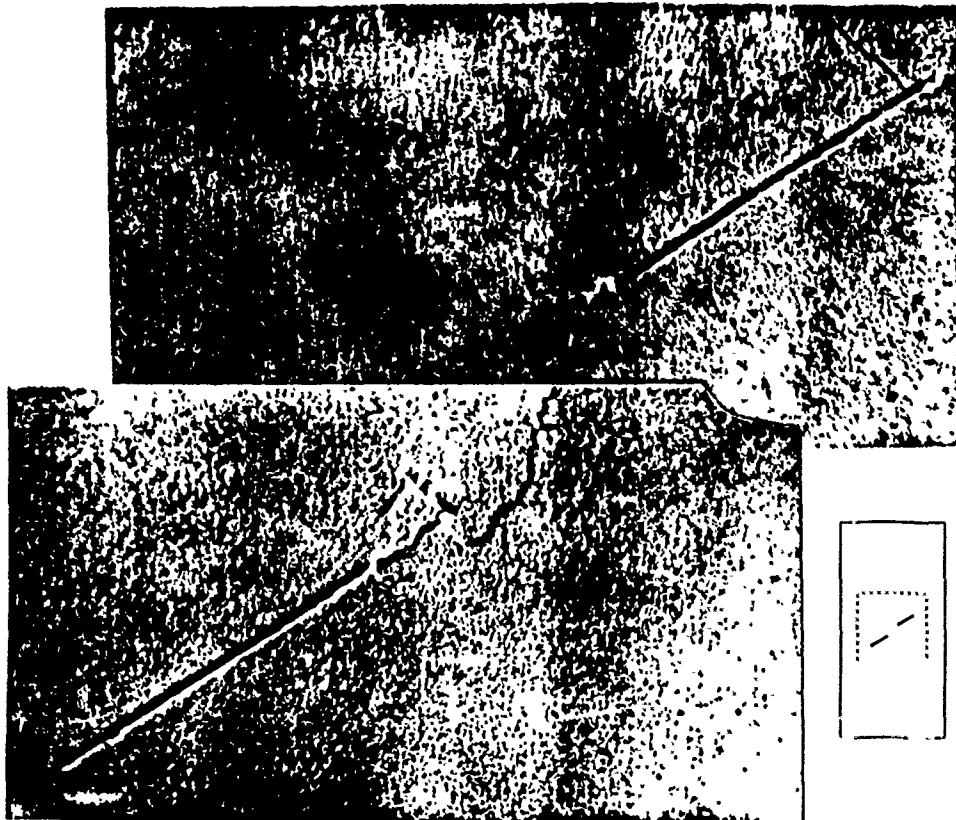


Figure 2.9. Uniaxial Compression Test on  $30^{\circ}$ - $45^{\circ}$  Specimen, (Same test as shown in Figs. 2.5-2.7), Overall View  
Note: Open external wing cracks, closed internal wing cracks and secondary coalescence crack.

Volume I. Figure 2.10 shows a plot of the observed coalescence loads versus rock bridge orientation angle for non-overlapping fractures. Triangular, square and circular symbols refer to fracture geometries with fractures that are inclined at  $30^\circ$ ,  $45^\circ$  and  $60^\circ$  with respect to the horizontal. The following can be deduced from Figure 2.10: (1) measured coalescence loads for specimens with the same fracture geometries are practically identical (two were tested for each geometry) confirming the repeatability of the observed coalescence phenomenon, (2) for the same rock bridge orientation angle, coalescence loads increased with increasing fracture inclination angle, and (3) for the same fracture inclination angle, coalescence loads were lowest for the rock bridge orientation angle of  $75^\circ$ . These trends had to be reproduced with our analytical model which will now be discussed.

### 2.3. Analytical Modelling of Fracture Coalescence

#### 2.3.1 Basic considerations and initial modelling

The stress/strain fields within the rock bridge after wing crack growth and just prior to secondary crack growth had to be established in order to understand the mechanisms underlying the fracture coalescence observed in the experiments. Stress analyses were thus performed using the finite element method and assuming linear elastic conditions ( $E = 6200$  MPa,  $\nu = 0.28$ ). The latter was a reasonable assumption since the load-displacement curves showed linear elastic behavior up to the point of brittle failure.

A major finding in these linear elastic stress analyses was that tensile stresses within the rock bridge were not relieved by wing crack growth, as can be seen by comparing Fig. 2.11 (a) and (b) which are vector plots of tensile major principal stresses around  $30^\circ$ - $75^\circ$  fractures before and after wing crack growth, respectively. The tensile stresses in the rock bridge zone in Fig. 2.11 (b) indicate that crack initiation within the rock bridge would not be surprising at all for materials such as rock which are weak in tension.

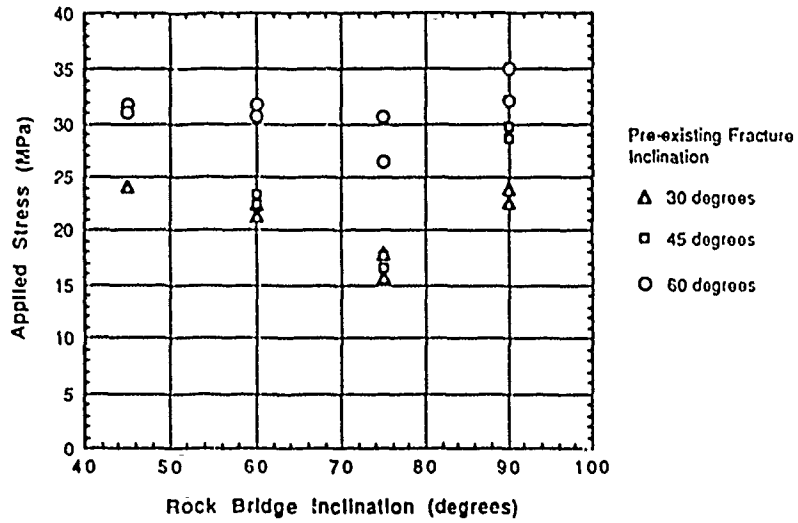
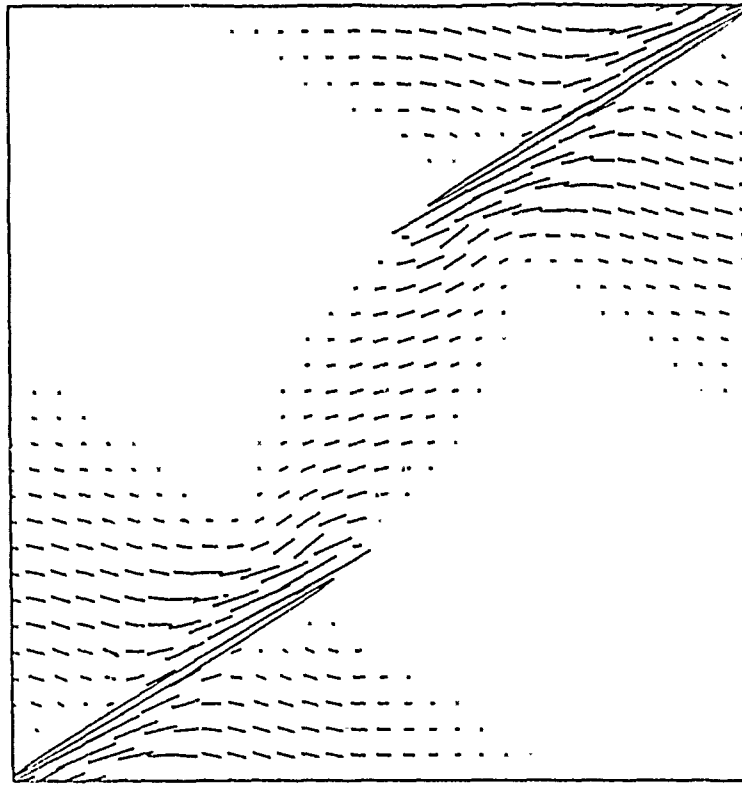


Figure 2.10. Uniaxial Tests on a Variety of Specimens with Two Non-overlapping Fractures



— Scale: Applied Vertical Compressive Stress

Figure 2.11a. Maximum Tensile Principal Stress Vectors of Specimen with  $30^{\circ}$ - $75^{\circ}$  Pre-existing Fractures Subject to Uniaxial Compressive Stress in Vertical Direction (before wing crack growth).

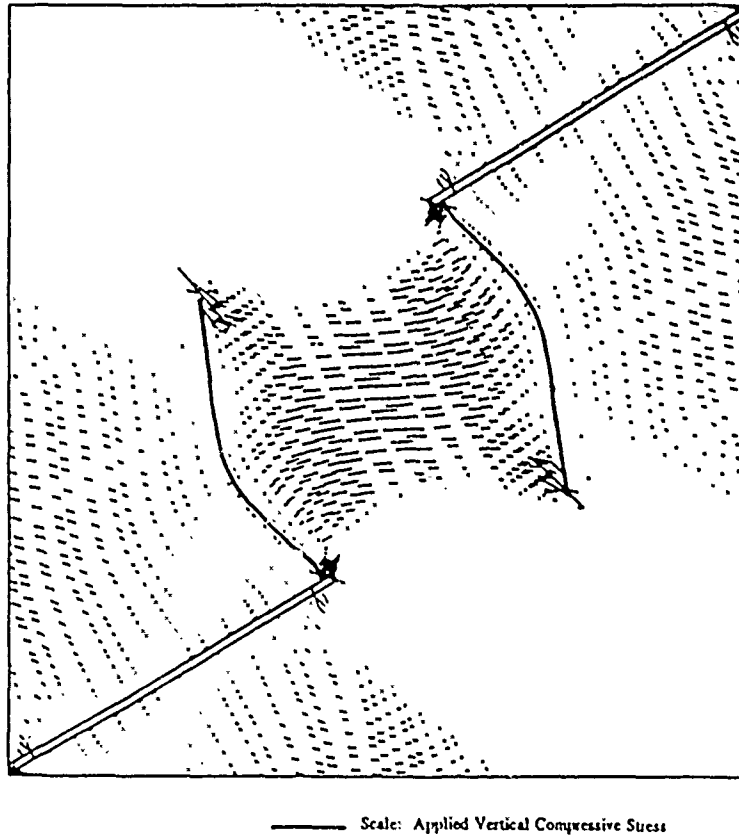


Figure 2.11b. Maximum Tensile Principal Stress Vectors of Specimen with  $30^{\circ}$ - $75^{\circ}$  Pre-existing Fractures and Internal Wing Cracks Subject to Uniaxial Compressive Stress in Vertical Direction  
Note: High tensile stress level in zone between wing cracks.

Given the existence of tensile stresses within the rock bridges where secondary crack growth occurred, it seemed obvious to apply a crack propagation criterion based on tensile stresses such as those discussed in the introduction. However, a more careful study of the contour plot of major principal stresses around the  $30^{\circ}$ - $45^{\circ}$  fractures, shown in Fig. 2.12, made us believe that a tensile stress-based criterion was not appropriate for simulating the fracture behavior in the experiments. Specifically, there were regions of high tensile stresses in areas outside of the rock bridge where no cracking was observed. On the other hand, a contour plot of major principal strains (Fig. 2.13) shows regions of high tensile strains only in areas where cracking occurred, such as close to the fracture tips and within the rock bridge (see Fig. 2.8). Given that regions of high tensile strains better correspond to the observed secondary cracking, we chose to use the maximum tensile principal strain rather than the maximum tensile principal stress as a basis for a fracture criterion. (It must be emphasized that in multiaxial stress fields the maximum principal strain is not simply proportional to the maximum principal stress in the same direction. Tensile principal strains can thus be higher for regions where there is a combination of large tensile and compressive principal stresses.) It is interesting to note that strain-based failure criteria can account for tensile failure (due to tensile strains) under biaxial (triaxial) compression even in a continuum. This is in contrast to tensile failure based on stress criteria which requires the existence of microcracks.

### 2.3.2 Simulating Crack Coalescence Using a Strain-based Smear- ed Crack Model

In modelling fracture coalescence, two possible approaches may be taken: (1) the discrete crack approach where the stress field around a crack tip coupled with a propagation criterion determines whether a crack will lengthen and in what direction it would extend and (2) the smeared crack approach where fractures are assumed to occur in locations of high stress or strain concentration. We combined the smeared crack approach with a stiffness degradation

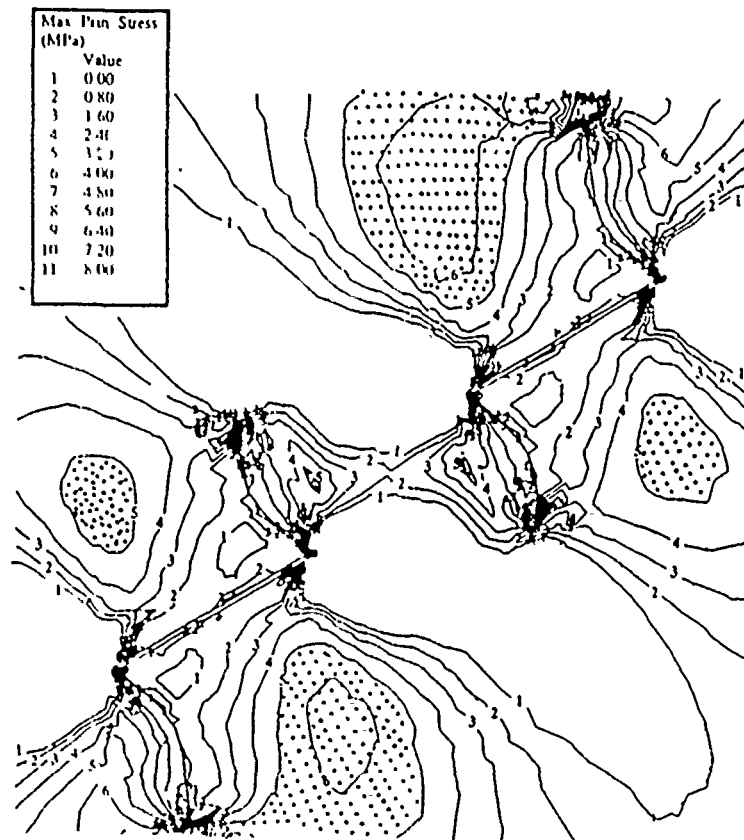


Figure 2.12. Maximum Tensile Principal Stress Contours for Specimen with  $30^{\circ}$ - $45^{\circ}$  Pre-existing Fractures at an Applied Uniaxial Compressive Load of 24 MPa. Dotted Areas Indicate Regions of High Tensile Stress.

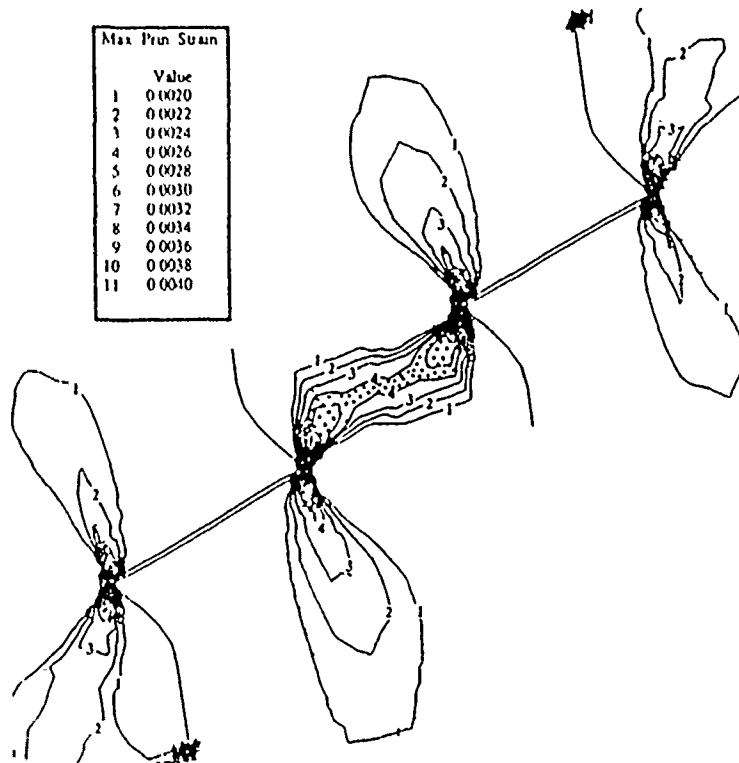


Figure 2.13. Maximum Tensile Principal Strain Contours for Specimen with 30°-45° Pre-existing Fractures at an Applied Uniaxial Compressive Load of 24 MPa. Dotted Areas Indicate Regions of High Tensile Strain.

occur in locations of high stress or strain concentration. We combined the smeared crack approach with a stiffness degradation model ("damage" model) [Rots et al., 1985; Lemaitre, 1986]. This is admittedly a simplification of the actual micromechanical process which seems to be justified at the present stage where the understanding of the actual propagation process is limited (see Section 2.2.2).

The stiffness degradation model which we have used to simulate fracture coalescence is defined as follows [Simo and Ju, 1987]:

$$\sigma_{ij} = (1-D) C_{ijkl} \epsilon_{kl} \quad (2.1)$$

where  $\sigma_{ij}$ ,  $\epsilon_{kl}$  and  $C_{ijkl}$  are components of the stress, strain and elastic constitutive tensors, respectively, and  $D$  is an internal state variable which measure the damage in the material.  $D$  ranges from 0 to 1 corresponding, respectively, to a material having the original elastic stiffness (i.e., "no damage") to one having zero stiffness (i.e., "completely damaged"). In our approach in which we use a strain dependent criterion  $D$  is dependent on an equivalent strain  $\epsilon_{eq}$ ,

$$D = \begin{cases} 0 & \text{for } \epsilon_{eq} < \epsilon_o \\ H(\epsilon_{eq}) & \text{for } \epsilon_o \leq \epsilon_{eq} \leq \frac{\epsilon_o}{A} \\ H\left(\frac{\epsilon_o}{A}\right) & \text{for } \frac{\epsilon_o}{A} \leq \epsilon_{eq} \end{cases} \quad (2.2)$$

where

$$H(\epsilon) = 1 - \exp\left[A\left(1 - \frac{\epsilon}{\epsilon_o}\right)\right] \quad (2.3)$$

and the equivalent strain is taken as [Lemaitre, 1986]:

$$\epsilon_{eq} = \begin{cases} \epsilon_1 & \text{for } \epsilon_1 > 0 \\ 0 & \text{for } \epsilon_1 \leq 0 \end{cases} \quad (2.4)$$

rate at which  $D$  increases with strain. Eq. (2.3) also implies that the damage has a maximum value of  $H(\epsilon_0/A)$  which will be referred to as  $D_{sat}$  (saturation value) in the subsequent discussion.

The model described above was implemented as a material subroutine for ABAQUS [ABAQUS User's Manual, 1990]. Simulations were performed on "edge" models (see Fig. 2.14) which were thought to be adequate for investigating coalescence crack growth in the rock bridge. Using edge models required less computation time due to the smaller number of finite elements when compared to the "full" models. (The elastic strain fields within the rock bridge of the edge models were similar to those obtained from the full model.) To obtain the parameters  $\epsilon_0$  and  $A$ , we went through several calibration cycles using the  $30^\circ$ - $75^\circ$  fracture geometry. In other words, we estimated  $\epsilon_0$  and  $A$ , calculated the corresponding parameter  $D_{sat}$  and used the finite element model with these parameters to compute the applied load at which  $D_{sat}$  is reached within the entire rock bridge. This computed load was compared to the measured load. This calibration led us to chose  $\epsilon_0 = 0.0024$  and  $A = 0.785$  corresponding to a  $D_{sat} = 0.19$ . We then used the same parameter values for other geometries. The computed and experimentally obtained loads for all non-overlapping geometries are shown in Fig. 2.15. As this figure shows, there is a satisfactory agreement between the experimental and computed values with discrepancies that are roughly the same for all geometries.

#### 2.4 Concluding Comments and Outlook

The research on fractures of fractured rock revealed that pre-existing fractures coalesce in two different modes depending on their geometry. If the pre-existing fractures overlap, they coalesce through interconnection of the developing wing cracks; if the pre-existing fractures do not overlap, coalescence occurs through secondary cracks which occur in addition to and after the wing cracks. Such fracture coalescence has not been observed so far, and, consequently, no analytical prediction model exists. (As a matter of fact, fracture coalescence analysis for overlapping pre-existing fractures only predicts wing crack geometry but not the actual

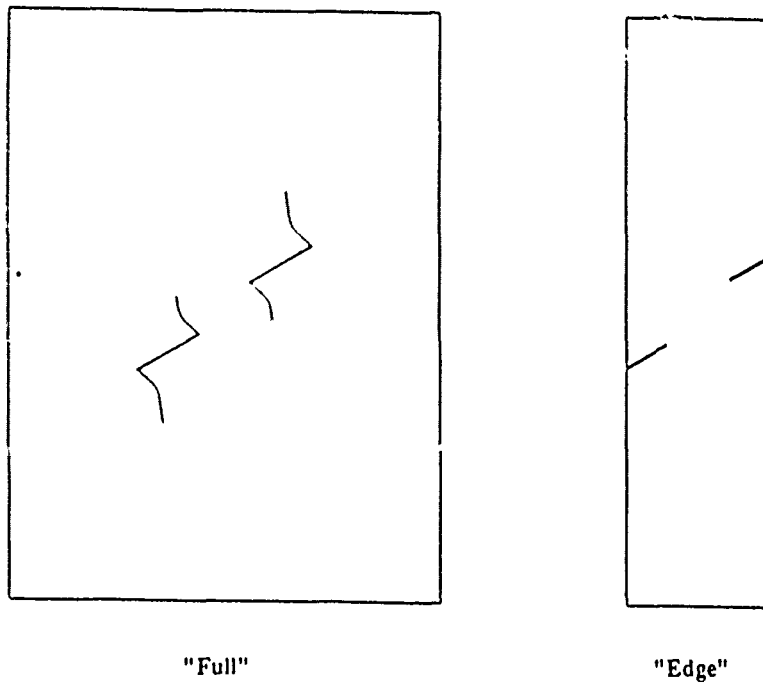


Figure 2.14. Geometry of Full and Edge Models

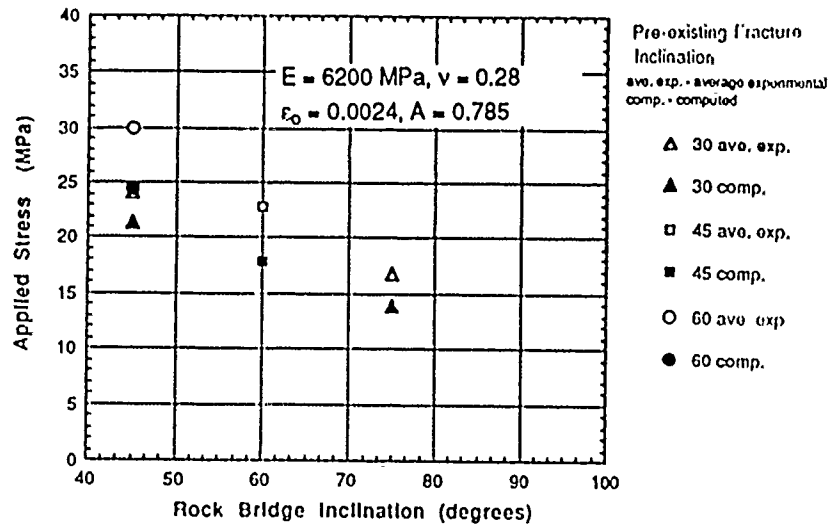


Figure 2.15. Comparison of Experimental and Analytical Results for Uniaxial Tests on Specimens with Non-overlapping Pre-existing Fractures

coalescence.) The coalescence of non-overlapping fractures occurs at loads which are lower than those for overlapping fractures with otherwise identical geometries. For this reason, we developed a new analytical model which we validated successfully.

These experimental and analytical results represent thus a significant breakthrough which is not only important for fractured rock but for any brittle material with pre-existing discontinuities such as cracks or fractures. The results are potentially very relevant to the representation of behavior varying from microcrack coalescence in brittle materials to fracture and fault coalescence in geology.

Clearly, only a first step has been made in this research. Numerous issues remain to be resolved. Experimentally it is necessary to consider other materials and other fracture geometries. Eventually we will also have to consider more complex loading conditions and the possibility that different types of fracture coalescence occur simultaneously or in interrelated sequence. Experiments would probably gain from whole field measurement technology such as holography and speckle interferometry.

Analytically one would like to eventually model the process in more detail. In particular, it would be desirable to represent crack propagation considering the combination of tensile fractures and shear fracturing that evidently takes place.

### 3. Centrifuge Modelling

#### 3.1 Problem Statement and Research Schedule

The great advantage of centrifuge modelling is the possibility to apply stresses at levels corresponding to reality, and which are geostatically distributed in the model. In preparation for the present research, we have conducted an extensive study of scaled modelling and of centrifuge testing in rock mechanics [Literature Review of Geotechnical Centrifuge Modelling with Particular Emphasis on Rock Mechanics, 1987 by Joseph, Einstein, Whitman and Rock Modelling Using the Centrifuge, 1987 by Joseph and Einstein]. These studies have confirmed the questions raised about the applicability of centrifuge testing in modelling of jointed rock, i.e. in modelling of discontinua. The questions arise from the possibility that discontinuum behavior may depend on absolute displacements. Since the displacements in the centrifuge are scaled at the ratio of model to prototype geometry, they are smaller than the prototype displacements. If absolute displacements govern the behavior, a centrifuge test will therefore, not correctly model the real behavior, if the same material is used for model and prototype.

One of our objectives in this research was thus to determine the applicability of centrifuge modelling for discontinua through a so called "modelling the model" approach. In this approach the behavior of differently scaled models of the same prototype is compared. If absolute displacements (or other absolute characteristics) rather than scaled displacements govern the behavior, this will become apparent. The problem we chose to study is arching behavior of a jointed rock mass using the classic trapdoor experiment.

An obvious starting point for trapdoor arching tests with jointed material were analogous tests with granular material. This would allow us to compare, and thus in a way calibrate our trapdoor experimentation with the many trapdoor experiments on granular material which have been performed under normal gravity. It also provided a basis for comparison with the few centrifuge trapdoor experiments on granular material conducted by others. Differences between trapdoor 1-g and elevated g experiments with such material

would have significant implications on analysis and design approaches which are based on arching. Following the trapdoor studies on sand were those involving a discontinuum i.e a jointed rock model. As mentioned before this would allow us to investigate the applicability of centrifuge testing to model discontinua. It would also provide us with better knowledge on arching behavior in such materials. As a final problem area in this research, we studied the arching concept and related theories. The intention was to reconcile our experimental observations with the existing theories and, if necessary, develop a new or modified theory.

The first year of this research project was devoted to the development of a trapdoor setup in the centrifuge and to conducting initial tests with sand (see "Stochastic and Centrifuge Modelling of Jointed Rock, Annual Report, 1987/88). In the second year of research (see "Stochastic and Centrifuge Modelling of Jointed Rock", Annual Report 1988/89) we modified the experimental setup based on our initial sand experiments and conducted the remainder of the sand experiments. We also started the tests on discontinua (jointed rock) which was also the main topic of the third year research. During this third year we also conducted tests on a scaled granular substance, namely, glass beads of different sizes. During the second and third year, parallel research at the Ruhr University, Bochum, was performed on jointed rock with a somewhat larger trapdoor and joint spacing. (This research which was funded by German sponsors, enhanced our modelling the model approach and led to a paper, "Trapdoor Experiments With Simulated Jointed Rock", Iglesia, et al., by both research groups.)

## 3.2 Experimental Arrangement

### 3.2.1 MIT Setup and Calibration

The essential features of the experimental apparatus at MIT are presented in Figure 3.1. The movement of the trapdoor was achieved by means of a system of wedges. The lower wedge was pulled by a motor-driven rod through a gear box assembly, causing the upper wedge, which is restrained laterally, to slide down at a vertical displacement rate of 0.018 mm/sec. The vertical force on the

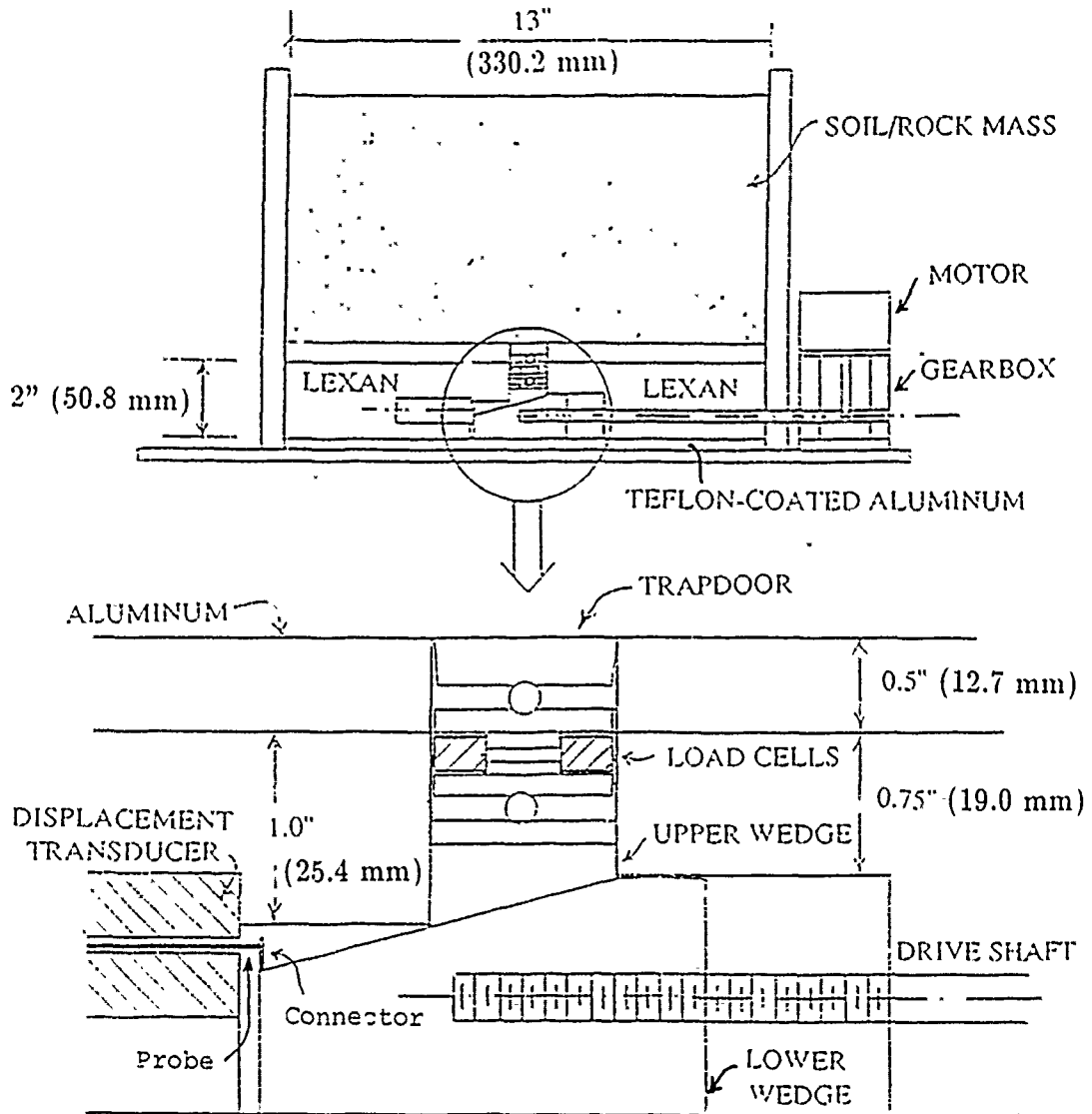
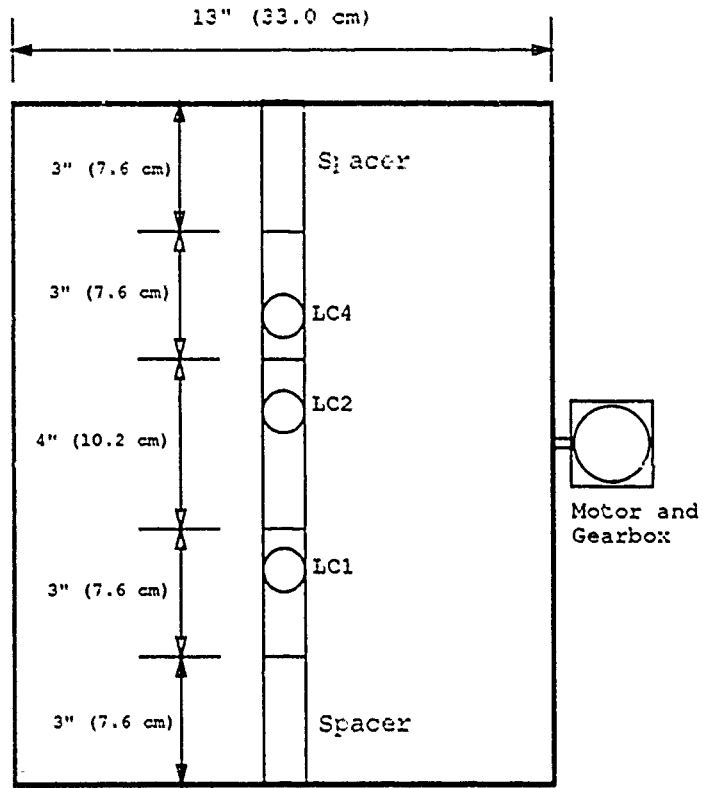


Figure 3.1: MIT Trapdoor Apparatus

trapdoor was measured by load cells installed between the trapdoor and the upper wedge. The displacement of the door was monitored by a transducer, the probe of which was attached to the lower wedge through a tiny piece which protrudes vertically at the toe of the wedge. (Note that the measured displacement was the horizontal movement of the lower wedge; the vertical translation of the trapdoor can be computed from simple geometric relations.)

The trapdoor strip consisted of three aluminum segments, each 6.35 mm thick and supported by a ball and a roller, as shown in Figure 3.2. One segment, 4 inches (101.6 mm) in length, has been placed in between two shorter segments, each 3 inches (76.2 mm) long. The balls transmitted part of the door load onto the load cells through cylindrical steel caps which were positioned right at the center of each load cell. (To ensure a truly concentric loading, another set of balls and steel caps were installed underneath the center of each load cell.) The roller support was located almost at the end of each segment, while the ball support (atop a load cell) was situated at a third of the segment span from the other end. The edges of the trapdoor segments have been tapered slightly so as to minimize friction with the side walls of the trench. In the absence of other measurements related to the door load, a critical assumption being made in the reduction of the data was that the resultant force due to the earth pressure acts at the center of each door segment.

A number of calibration experiments were run with this setup consisting of runs with no load and with calibrated masses on the trapdoor. After initial tests with sand indicated that the stiffness of the door may be different from that of the adjacent base, a special series of tests was run to investigate this. As it turned out, the door was stiffer than the adjacent base and "attracts" thus more load before the trapdoor is lowered. This explains why the load displacement curves in our tests started at loads which are greater than the theoretical load  $N_{gph}$  ( $N_g$  = acceleration in multiples of gravity,  $\rho$  = density,  $h$  = overburden depth). A correction was easily possible by shifting the load displacement curve such that the theoretical load occurs at zero displacement, as illustrated in Figure 3.3. The shifting of the curve is apparent in Figure 3.3a and 3.3b.



Plan view

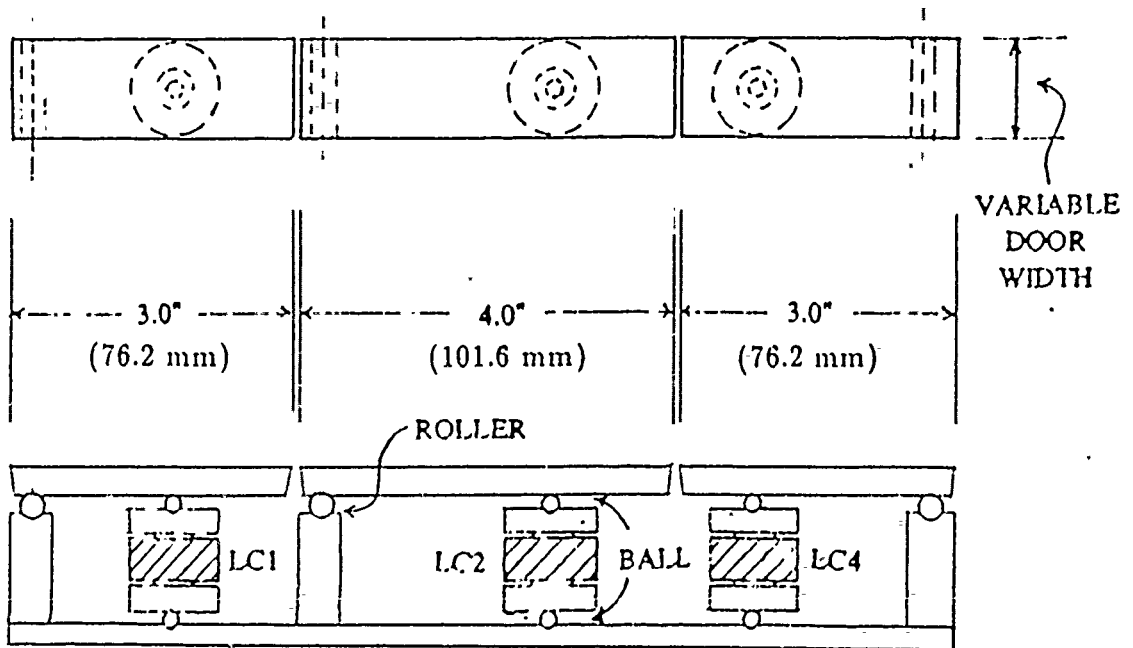


Figure 3.2: MIT Load Cell Setup

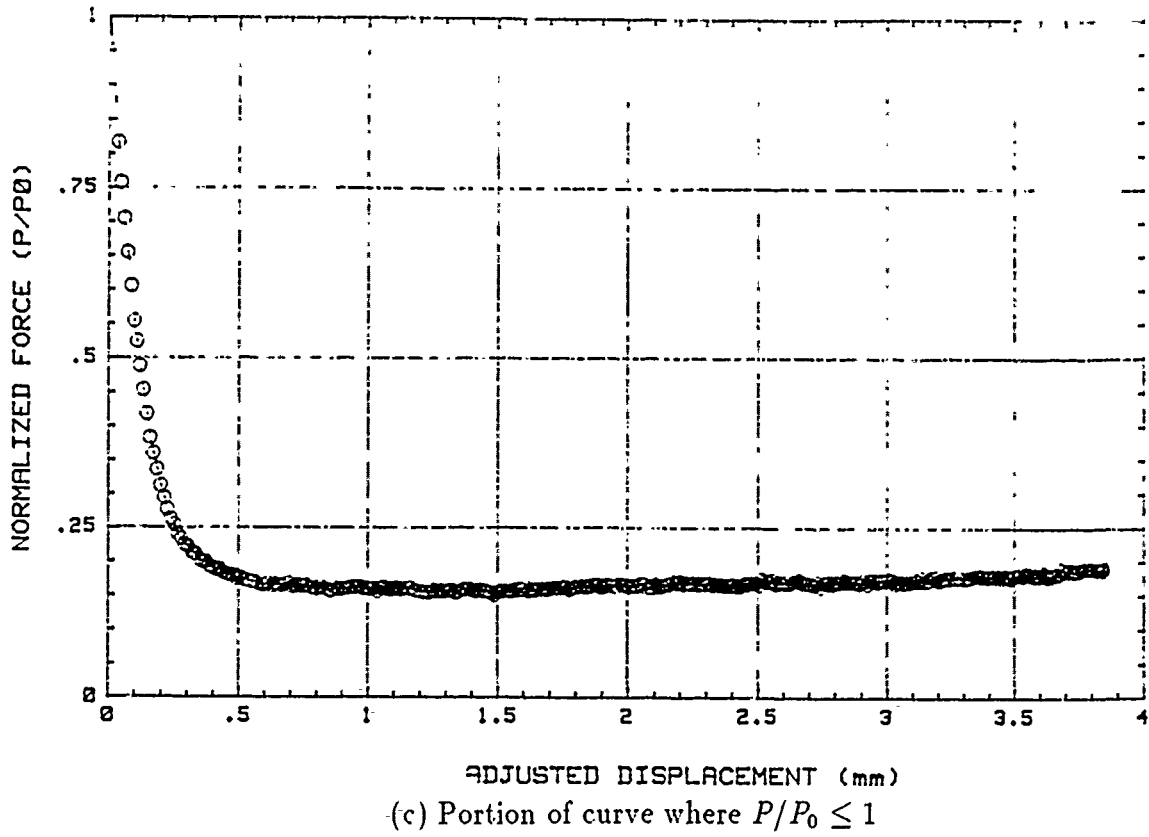
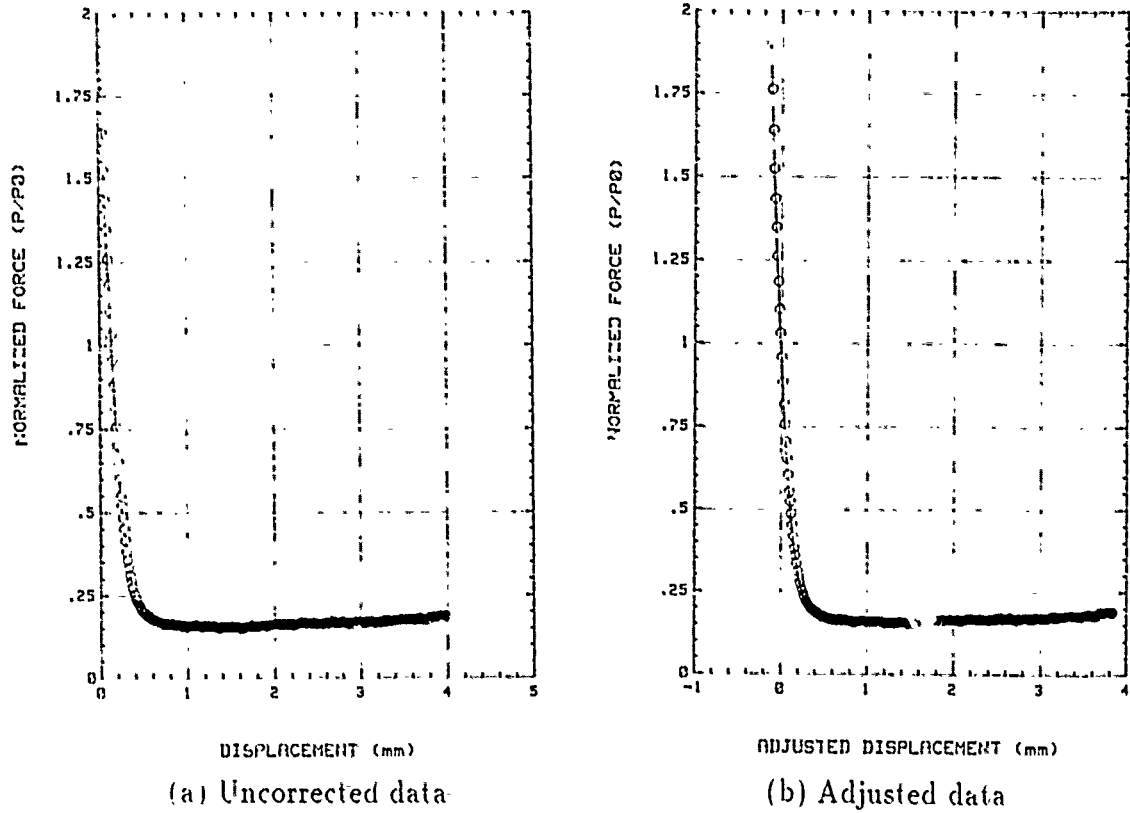


Figure 3.3: Correction of Load vs. Displacement Curve

The portion of the curve where the ratio ( $P/P_0$ ) of the measured load to the theoretical load is less than or equal to unity (Figure 3.3c) was then considered to be the correct curve in the active arching mode.

### 3.2.2 Ruhr University Bochum (RUB) Setup

The trapdoor system at RUB, depicted in Figure 3.4 was slightly different from the MIT arrangement. Movement was controlled by a hydraulic system connected to a piston which supported the trapdoor. To prevent premature piston settlement at the acceleration was increased prior to door lowering, back pressure was applied to the piston through a column of water contained in a medium-high pressure vessel. Before dropping the piston, the back pressure was cut off by closing the solenoid valve 1, and the piston was subsequently lowered by opening valve 2.

The front of the strong box was formed by a 70 mm thick perspex face through which deformations of the model were recorded on video cassette. In the RUB test package, there were four trapdoor segments, each 10 mm thick, 97.5 mm long, and also made of aluminum. The segments were designated number 1 through 4 from the front face to the back wall of the strong box. Only three of these - segments 1, 2, and 4 - were equipped with load cells, because segment 3 was instrumented with a displacement transducer to monitor the trapdoor movement. Each segment was simply supported as in the MIT setup, except that a "knife edge", was used instead of a roller.

## 3.3 Tests on Granular Material

### 3.3.1 Tests with Sand

For these experiments, New Jersey 4/14\* (coarse) sand with subangular grains (specific gravity  $G_s=2.66$ ) having an average size of 2.1 mm was used. The typical testing procedure as shown in Figure 3.5 consisted of applying the elevated gravitational level in four stages. Once the highest acceleration level was reached, the trapdoor

---

\* These numbers indicate the U.S. Standard sieve sizes through which the sand particles pass and on which they are retained. Thus, the sand used passes through the #4 (4.76mm) sieve and is retained on the #14 (1.41mm) sieve.

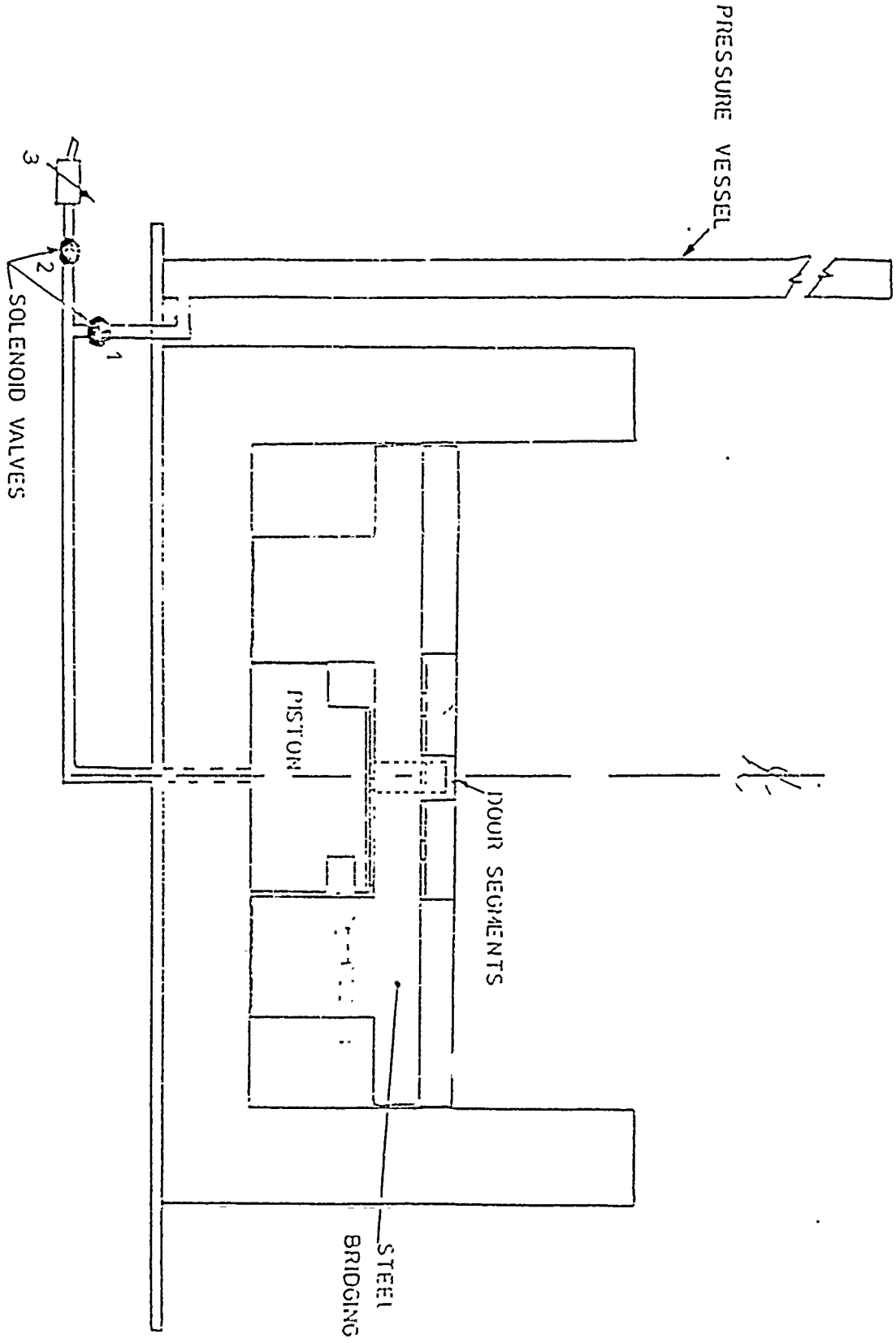
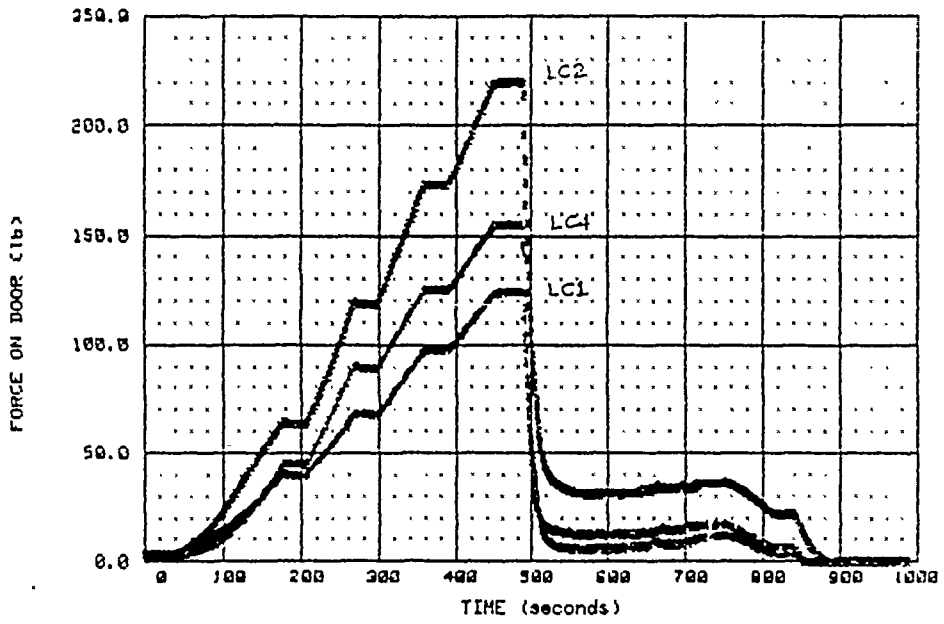
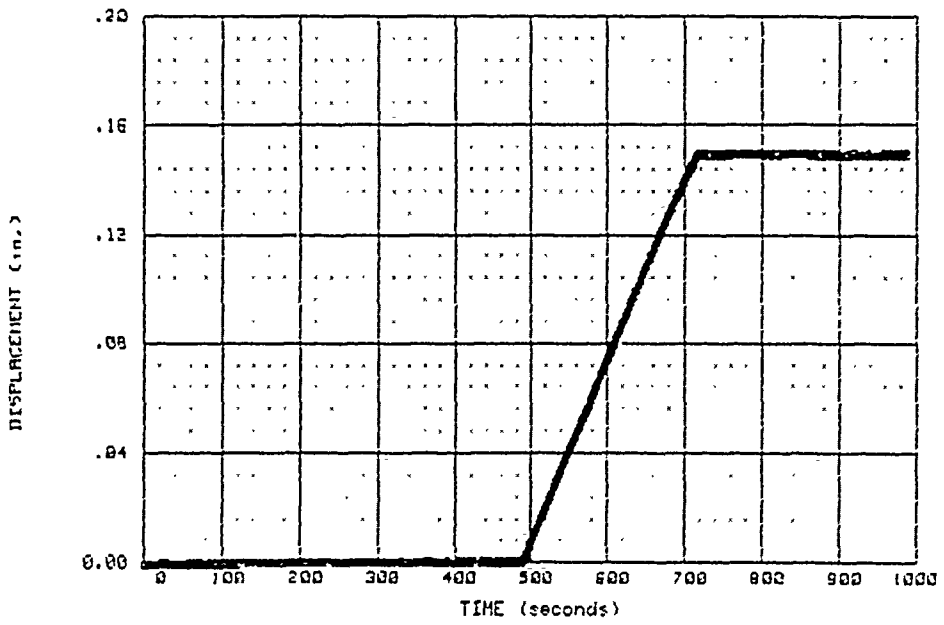


Figure 3.4: RUB Trapdoor Setup



TEST G1106: DOOR LOAD DATA



TEST G1106: DOOR DISPLACEMENT DATA

Figure 3.5: Typical Test Data

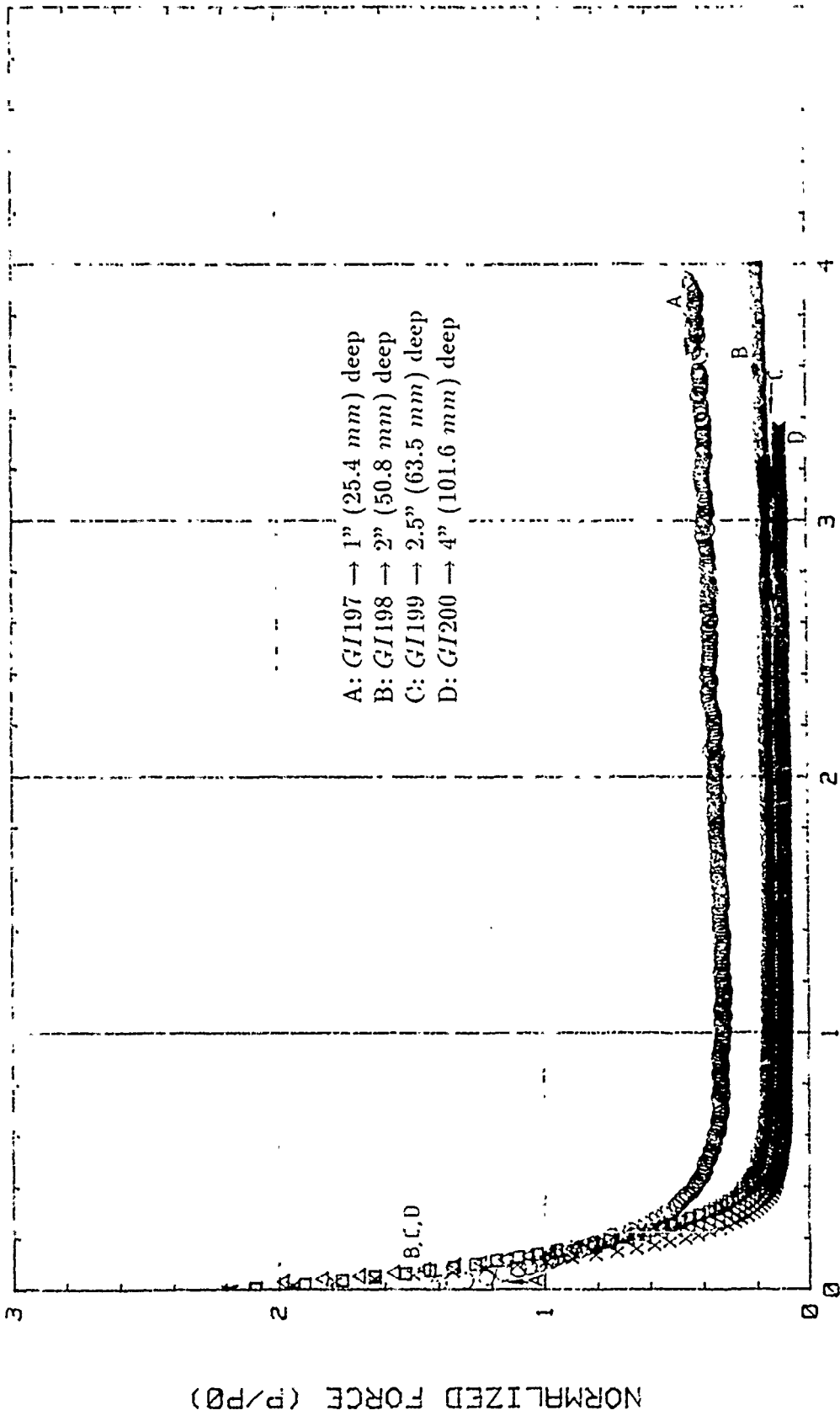
was moved down up to the maximum possible displacement of 4 mm. After this, the acceleration was reduced until the 1g level was reached.

The results showed the expected decrease of the trapdoor load as displacement increased. (Fig. 3.6 shows typical load displacement curve and it also indicates that the minimum load increased as the overburden depth decreased. This is entirely analagous to trapdoor experiments under normal gravity run by others (e.g. Terzaghi, 1936). The normalized displacement (i.e. displacement/trapdoor width) at which the minimum load occurred was about 0.02 for the centrifuge experiments and previous tests run under normal gravity by others. What was different in high g centrifuge testing was the fact that, after reaching the minimum load, the load increase with displacement was much less than in earlier normal gravity tests.

Modelling the model was investigated by properly scaling geometry and gravity level. As shown in Fig. 3.7 the corresponding curves, e.g. 2" overburden on 2" door at 40g compared to 1" overburden on 1" door at 80 g coincide.

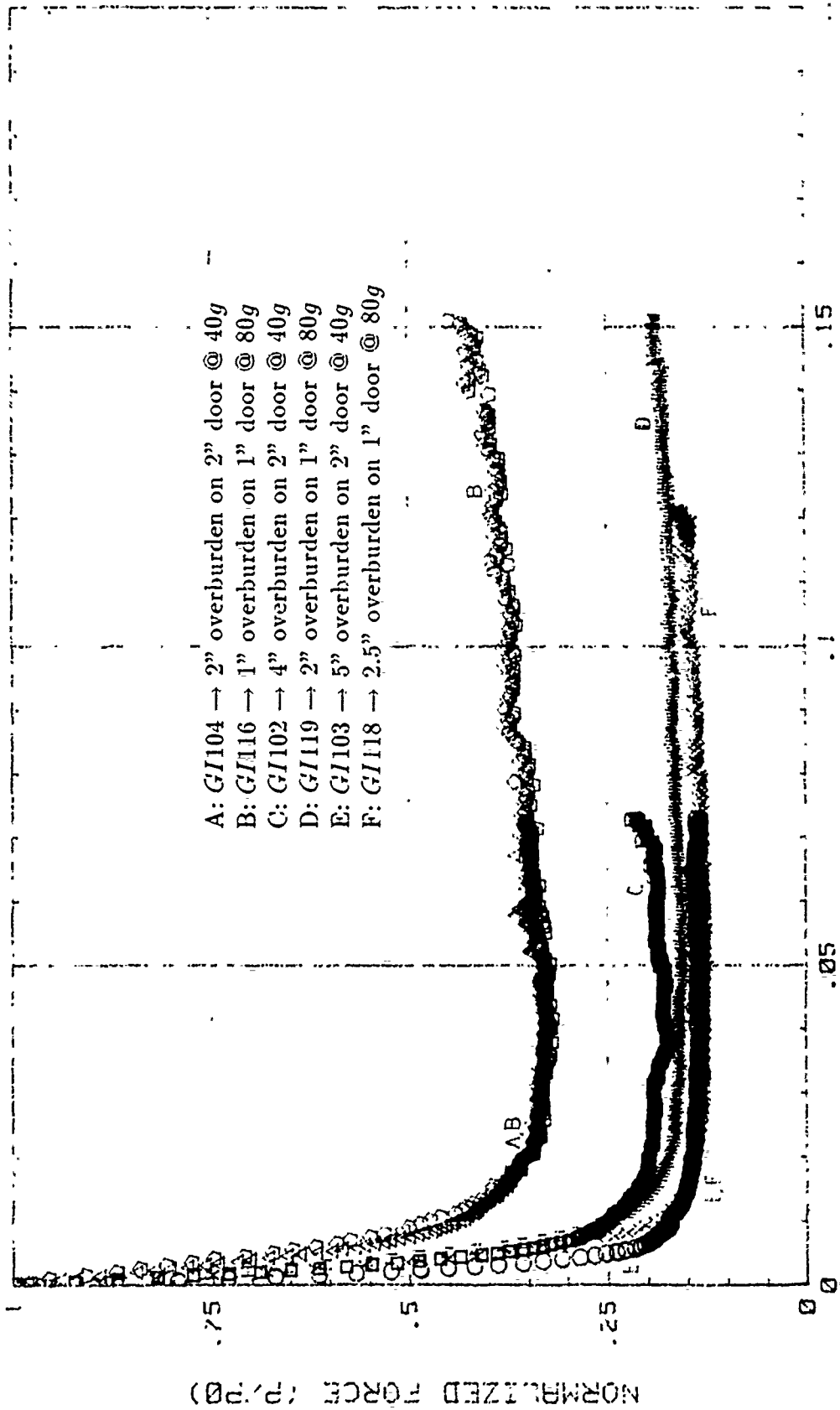
### 3.3.2 Tests with Glass Beads

Four different size glass beads with mean diameters of 0.5 mm, 1.5 mm, 3.0 mm and 6.0 mm were used. They were placed in the same manner as the sand, and the spinup, door lowering and termination of the centrifuge tests was identical to those on sand. When everything was scaled appropriately, the normalized force/normalized displacement curves in Fig. 3.8 coincided. This indicated that proper scaling should include the scaling of grain size. Subsequent tests were run in which either grain size was varied, while the trapdoor width was held constant and vice versa (door width varied, grain size constant); these tests indicated, however, that the scaling of the door size, i.e. of the "structure" is much more important than the scaling of the grain size.



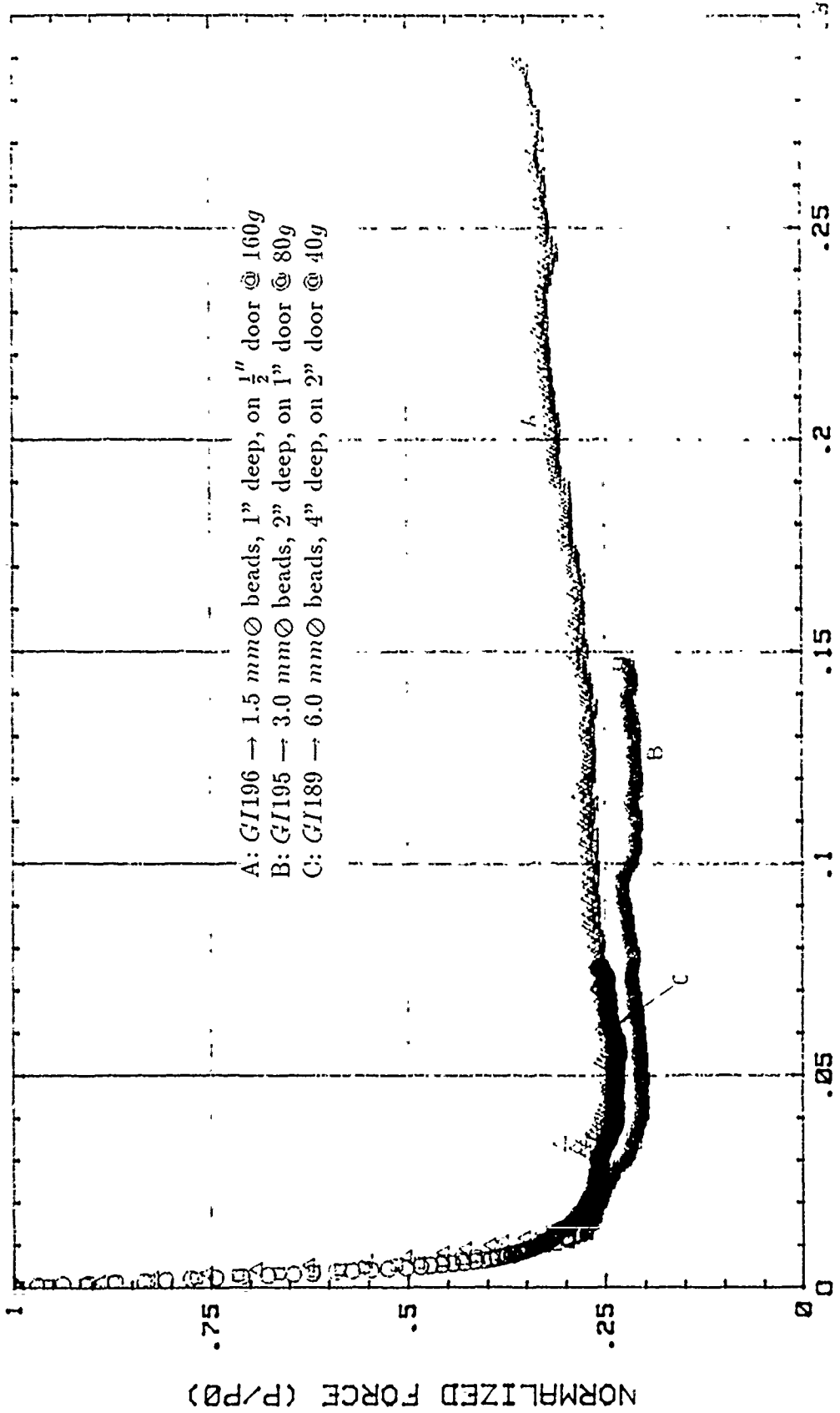
DISPLACEMENT (mm)

Figure 3.6: Tests with Coarse Sand of Varying Depths on 1" (25.4 mm) Door @ 80g



NORMALIZED DISPLACEMENT ( $d'/B$ )

Figure 3.7: Modelling of Models with Coarse Sand: Normalized Force vs. Adjusted Displacement  $d'$  Normalized with Respect to the Door Width  $B$



**NORMALIZED DISPLACEMENT ( $d'/B$ )**

Figure 3.8: Modelling of Models with Glass Beads: Normalized Force vs. Adjusted Displacement  $d'$  Normalized with Respect to the Door Width  $B$

### 3.3.3 General Observations on Centrifuge Tests with Granular Materials

As can be seen in the two preceding sections, the load displacement curves first dropped to a minimum load followed by a slowly increasing load, for both sand and glass beads. As a matter of fact, the displacement when the minimum load is reached was 1 to 2% of the door width and was approximately the same in all tests run by us in the centrifuge at various g levels and by others at normal gravity. What was different in the high gravity centrifuge experiments was the slower load increase after the minimum load compared to 1g experiments. Also significant was the fact that an actual arch seemed to form, this arch was initially curved ("gothic" arch) but became triangular as the displacements increased.

## 3.4 Tests with a Jointed Medium

### 3.4.1 Test Layout

Initial tests were run with balsa wood rods of square cross-section and dimensions of 1/4" and 1/2" square. The results scattered significantly and made these tests difficult to interpret. Nevertheless, arching effects occurred leading to a load reduction down to 25% of the original load.

The main test series on discontinua both at MIT and at RUB were run with aluminum rods. Ideally, the rods should be made of a rock-like material, but it is difficult to find one which can easily be cast or cut into small pieces of uniform size. Aluminum rods were used since they are readily available in sizes small enough such that a reasonable number of pieces fit on the relatively narrow trapdoor strip. Also, if the main concern is the particular displacement dependent shearing between planar surfaces of semi-rigid elements and not the fracturing phenomena, experiments with metal rods should provide meaningful results. Moreover, aluminum is well suited for simulating rock due to its high strength-to-weight ratio (ideal for modelling semi-rigid components) and a specific gravity of 2.66 which is not too different from that of rock.

The jointed rock models were composed of rods, square in cross-section, which were juxtaposed side by side and top of each

other to simulate joint sets with uniform spacing. Two types of stack-up schemes were implemented: one in which the rods were directly placed on top of one another, and the other in a staggered fashion like bricks (Figure 3.9). Following a "modelling-of-models" technique, different but geometrically similar sizes of small-scale models (i.e., aluminum rods) and of trapdoors were used with corresponding accelerations in the centrifuge. At MIT, the door widths were 2" (50.8 mm), 1" (25.4mm) and 1/2" (12.7mm) for the 1/2" (12.7mm) [ ] 1/4"(6.35mm)[ ], and 1/8" (3.18 mm)[ ] rods, respectively, and the tests were carried out at 40g, 80g, and 160g. The RUB tests are performed at 25g and 50g using corresponding door widths of 80mm and 40 mm for aluminum rods sizes of 20 mm [ ] and 10mm[ ], respectively. (Since the experimental setup in this study was presumed to be in plane strain, the dimensions along the length of the trapdoor were considered to be irrelevant and were, thus, not scaled.)

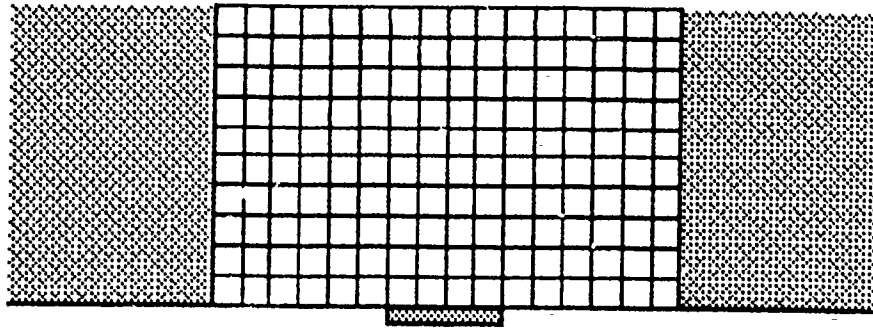
The lateral confinement of the aluminum rods was also standardized for both the MIT and RUB tests. Specifically, silica quartz glass beads, fairly uniform in size and with a specific gravity of 2.55, were placed on the sides. The use of glass spheres also allowed one to vary the diameter of the beads in accordance with the scaling of the rod and door sizes. The three glass bead diameters utilized at MIT were 6 mm, 3 mm, and 1.5 mm for the 40g, 80g, and 160g tests, respectively. At RUB, 5 mm diameter glass beads were used for the 50g experiments and, due to the unavailability of 10 mm diameter beads, for the 25g tests as well. A listing of the pertinent series of tests conducted at MIT and at RUB is given in Table 3.1.

#### 3.4.2 Direct Stack Tests

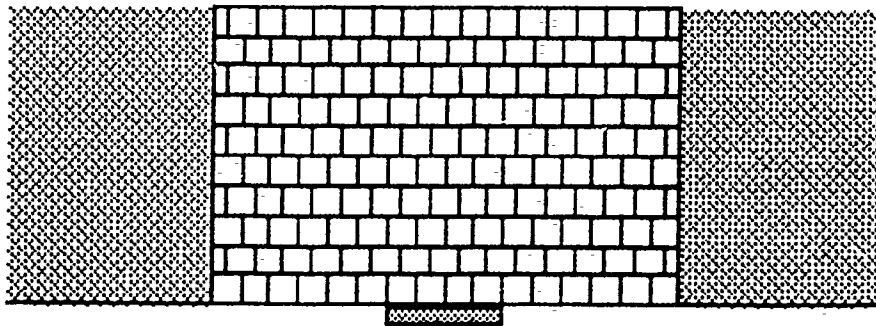
The results from the trapdoor experiments with the direct stack layout are displayed in Figures 3.10 and 3.11. The final configuration - the appearance of the blocky system at the end of each test resembles Figure 3.10. That is, the four columns of rods directly above the trapdoor simply followed the vertical door movement. In Figure 3.11, the measured force on the trapdoor,

	Rod Size	Total Height	Door Width	Glass Bead Size	Gravity Level
			M I T		
1.	$\frac{1}{2}$ in (12.7 mm)	5.00 in (127 mm)	2.0 in (50.8 mm)	6.0 mm	40g
2.	$\frac{1}{4}$ in (6.35 mm)	2.50 in (63.5 mm)	1.0 in (25.4 mm)	3.0 mm	80g
3.	$\frac{1}{8}$ in (3.18 mm)	1.25 in (31.8 mm)	0.5 in (12.7 mm)	1.5 mm	160g
			R U B		
4.	10 mm	100 mm	40 mm	5.0 mm	50g
5.	20 mm	200 mm	80 mm	5.0 mm	25g

Table 3.1. Testing Program



a. Direct Stack



b. Brick Stack

Figure 3.9: Jointed Medium Stack-up Patterns

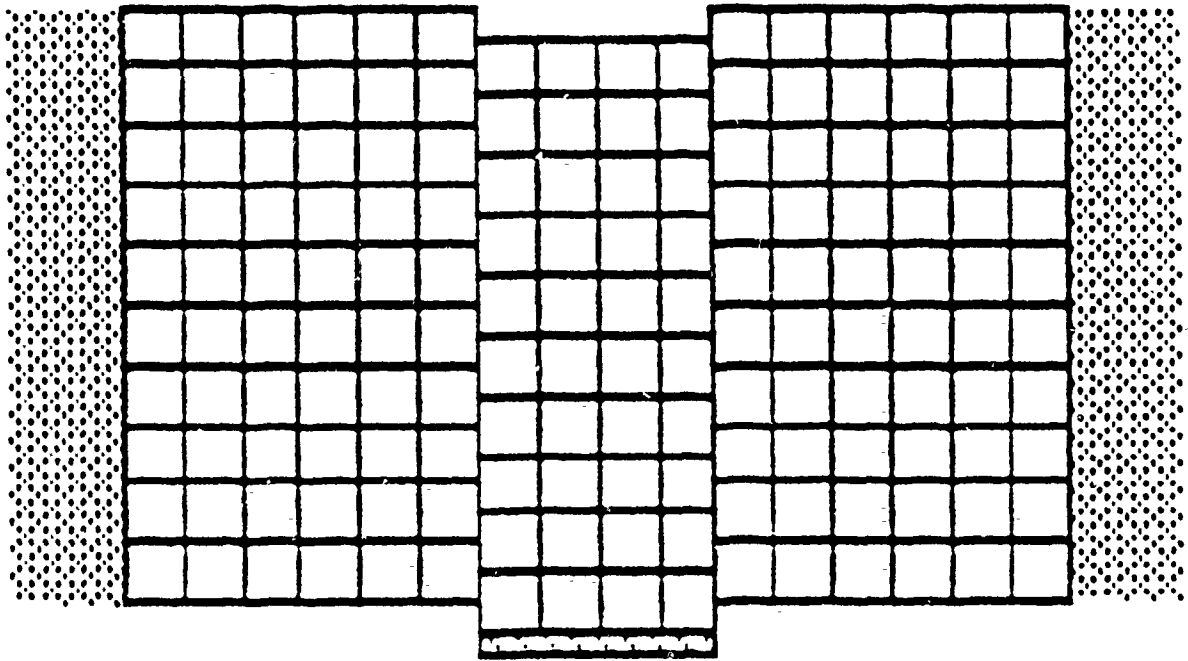


Figure 3.10: Direct Stack Tests: Final Configuration

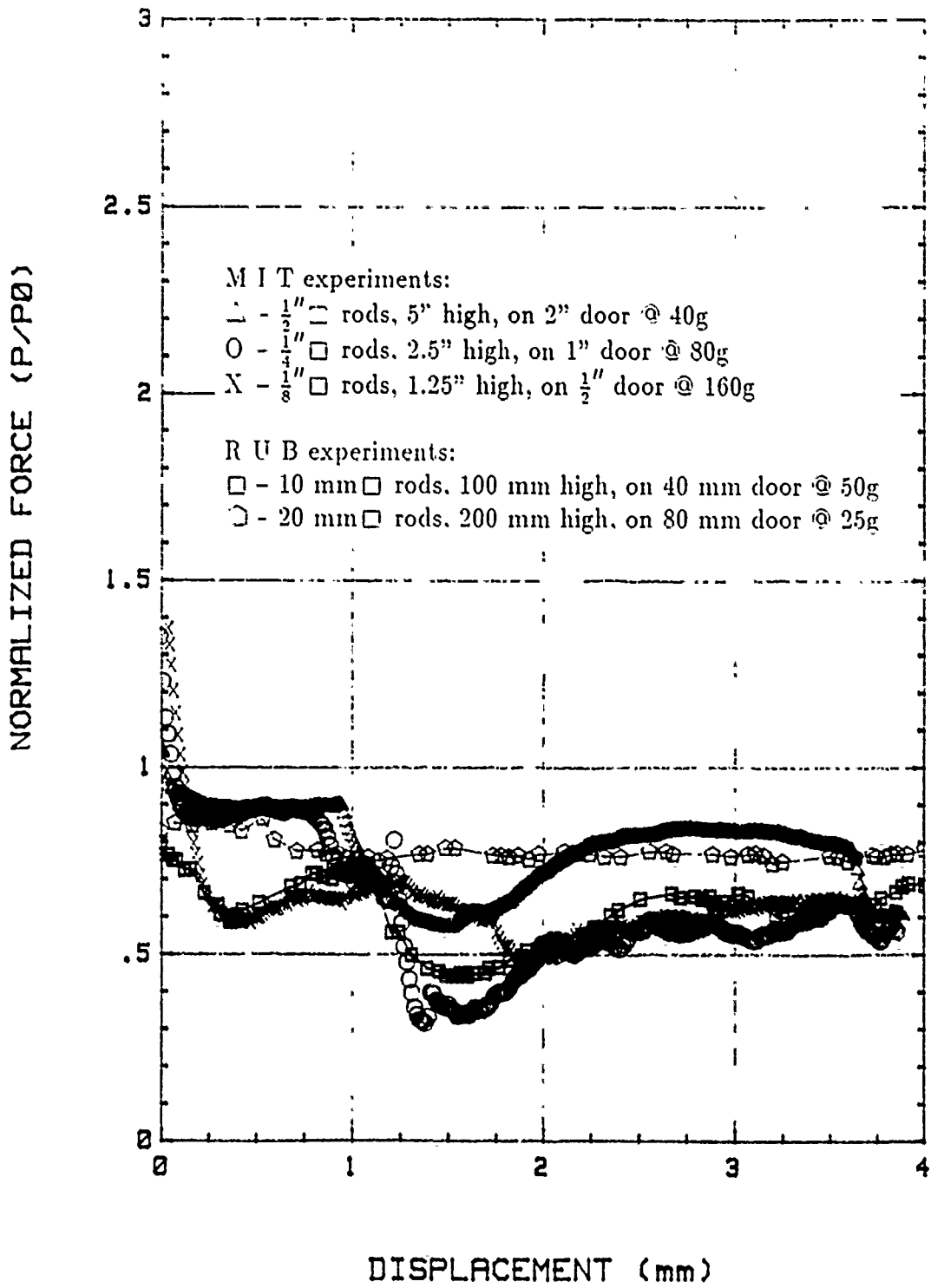


Figure 3.11: Direct Stack Tests: Normalized Load vs. Displacement Data

normalized with respect to the weight (at  $N_g$ ) of the material directly above the door, has been plotted against the vertical door translation for the various tests.

Note, in the MIT experiments, that the measured force on the door at zero displacement was greater than the theoretical geostatic force. This was caused by the greater stiffness of the trapdoor relative to the adjacent base as discussed in Section 3.2.1. The results show, with minor experimental scatter, that upon lowering of the door, an immediate reduction in load ensued. This was followed by a stage of approximately constant load up to a door displacement of 1 to 1.25mm, then a further decrease in load to about 1.5 mm displacement, and a gradual force increase toward another fairly constant value.

### 3.4.3 Brick Stack Test

For the brick stack cases, the results are given in Figures 3.12 and 3.13. In the final configuration (Figure 3.12), a triangular pattern is typically formed in the bottom four layers just above the trapdoor. This is reflected in the measured loads (Figure 3.13) which became constant towards the end of each experiment. The normalization of the forces in Figure 3.13 was done with respect to the theoretical geostatic weight of a volume of material above the door bounded by vertical planes passing through the edges of the door. A maximum of 40 blocks could be placed above the door, and the 10 rods that followed the door movement in each test constitute thus 25 percent of the theoretical geostatic force.

As the trapdoor settled in the brick stack case, the transition from the initial force to the minimum load followed a much smoother curve than in the direct stack experiment. It is evident from Figure 3.13 that the minimum load occurred at about the same amount of door displacement for all geometrically similar tests. This observation is even more pronounced if the data are adjusted such that zero displacement is taken where the normalized force ratio equals unity, shifting the curves in Figure 3.13 horizontally to those in Figure 3.14.

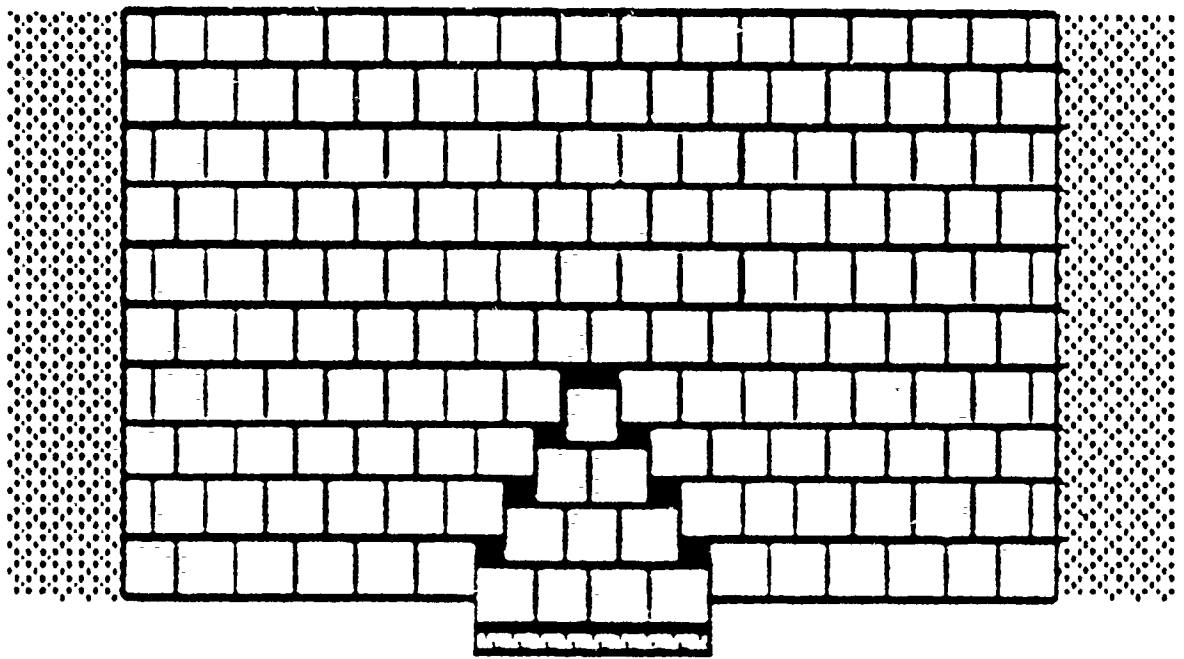


Figure 3.12: Brick Stack Tests: Final Configuration

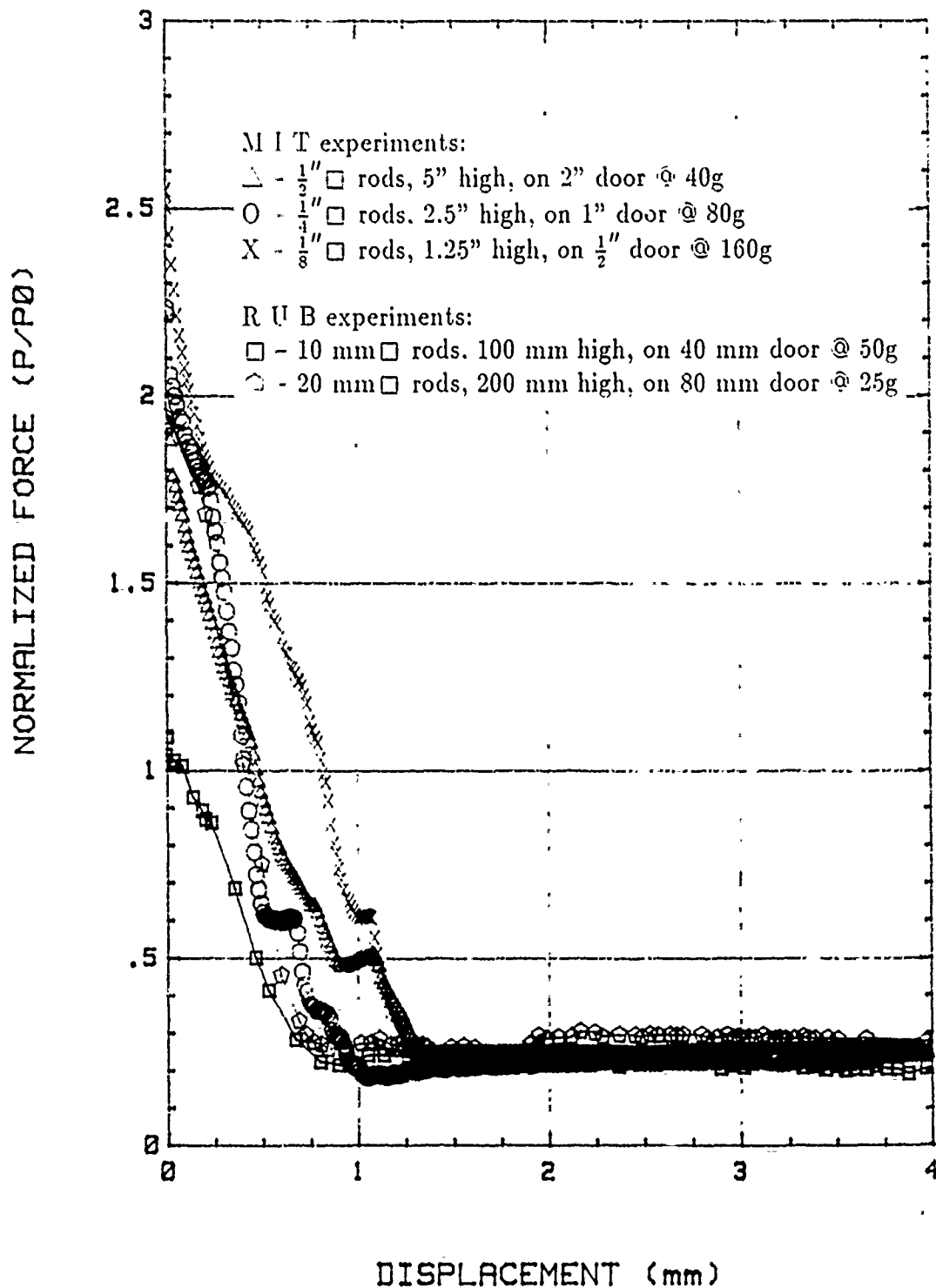


Figure 3.13: Brick Stack Tests: Normalized Load vs. Displacement Data

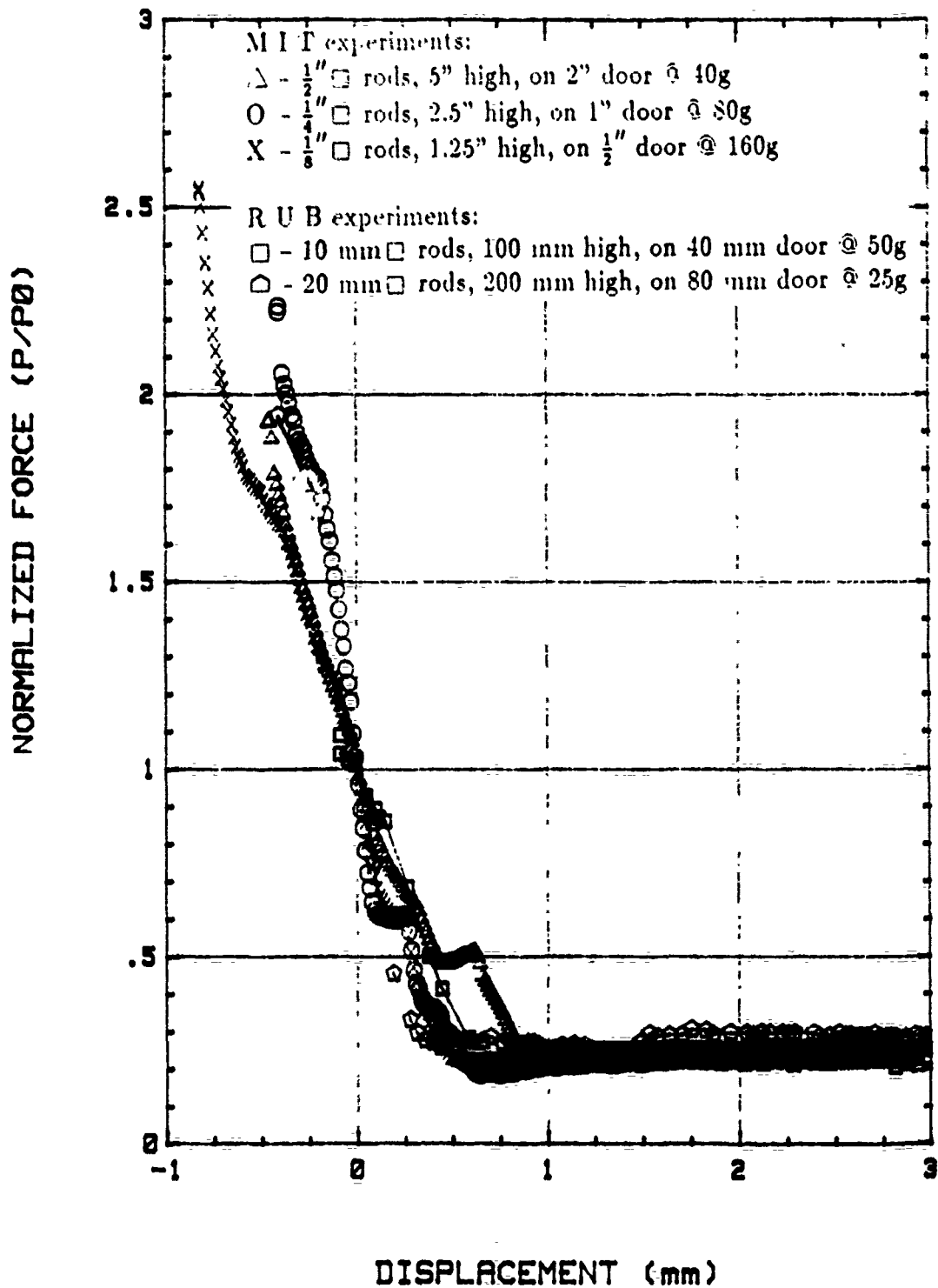


Figure 3.14: Brick Stack Tests: Normalized Load vs. Adjusted Displacement

#### 3.4.4 Interpretation of Tests Results

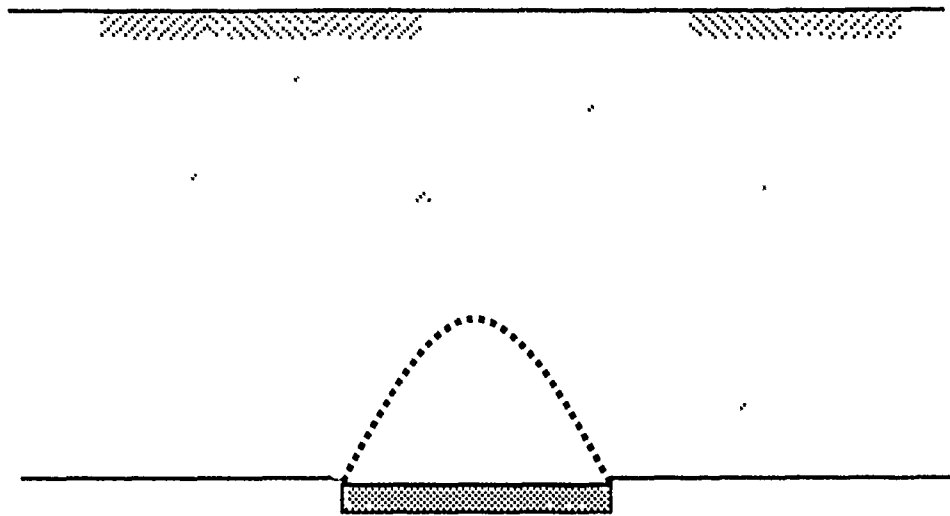
The results from the "modelling-of-models" exercise with discontinua showed that the geometrically similar setups at appropriately scaled g-levels exhibited similar load-displacement behavior in the trapdoor tests. The force values, especially the minimum loads, conformed approximately with the usual centrifuge scaling laws. However, these forces occurred at the same amount of absolute door displacement, in violation of the same scaling rules. Similitude requirements for scaling of length dimensions are simply not met by the observed displacements.

The fact that shearing depends on the absolute displacement between surfaces provides a serious obstacle to centrifuge experimentation on models involving discontinuities. It may be extremely difficult, if at all possible, to extrapolate results from model tests to actual prototype conditions unless the displacement dependence is also considered, possibly by scaling roughness on the discontinuity surfaces.

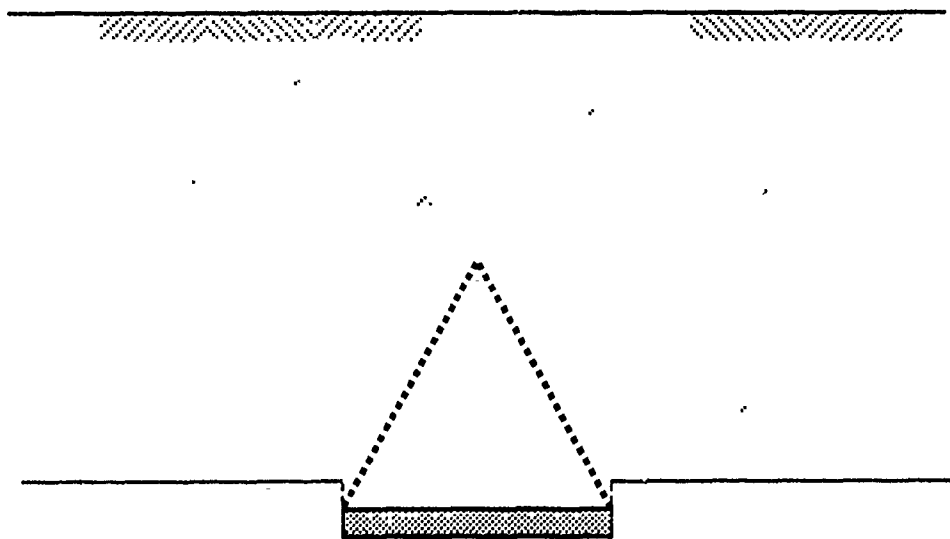
#### 3.5 Arching Theories

The settling of a trapdoor underneath a geomaterial produced an arch just above the door. The slope of this arch is initially parabolic Fig. 3.15a, then becomes triangular (3.15b). Eventually, at large trapdoor displacement, the arch collapses and a prismatic body (Fig. 3.16) of the overlying material follows the movement of the trapdoor. In our centrifuge experiments, which are limited to small displacements, we were able to observe the initially curved (parabolic) arch in both the sand and glass bead tests, as well as a transition to a triangular arch in the glass bead tests. Prismatic bodies at very large trapdoor displacements in centrifuge tests were observed by Stone (1988).

This mechanism of arching is consistent with well established relationships between (incremental) shearing strains and (incremental) volumetric strains in geomaterials. At small strains, a granular medium tends to dilate or increase in volume depending on the stress level and porosity. This ability of granular soils to carry shearing stresses brings about the formation of the arch above the



(a) Curved Arch



(b) Triangular Arch

Figure 3.15: Arching at Relatively Small Displacements

trapdoor, and considerable dilation of the soil occurs soon after the door is displaced. At large strains, the geomaterial tends to deform with hardly any change in volume. The eventual collapse of the arch leading to vertical failure surfaces is a manifestation of this stage of isochoric, or constant-volume, deformation.

The formation of an arch above a trapdoor or more importantly, above the crown of a tunnel has been observed or at least assumed in a number of analysis methods for tunnel support. Engesser (1881) and Bierbaumer (1913) assumed parabolic or triangular arches, respectively (Fig. 3.15) while Terzaghi worked with the ultimate prismatic body (Fig. 3.16). Evans (1983) developed an arching analysis based on observed triangular arching and rigorous consideration of plasticity theory (Volume II of this report series contains a detailed review of these and other theories). Predictions with these methods are compared in Table 3.2 (taking  $\phi=39^\circ$  as determined for the sand used on our centrifuge tests).

H/B	Engesser $K=K_a$	Terzaghi $K=1$	Evans $(K=1.2)$ $(P/P)_{\min}^2$	$(P/P_o)_{\text{ult}}$
1	$P/P_o$ 0.258	$P/P_o$ 0.495	0.309	0.516
2	0.133	0.297	0.154	0.315
4	0.068	0.168	0.077	0.182

Table 3.2. Comparisons of different theories applied to the centrifuge tests with sand: Computed values of force on trapdoor normalized with respect to overburden ( $P/P_o$ ). ( $K$ =Lateral earth pressure coeff.;  $K_a$ = active earth pressure coeff.;  $H/B$ =ratio of overburden height to trapdoor width)

In our tests the minimum normalized  $P/P_o$  forces were 0.36, 0.18, 0.09 for  $H/B=1,2,4$  respectively. Terzaghi's theory which is based on the ultimate load naturally produces larger loads. Of the other two, Evans predictions seem to be closer to our observations.

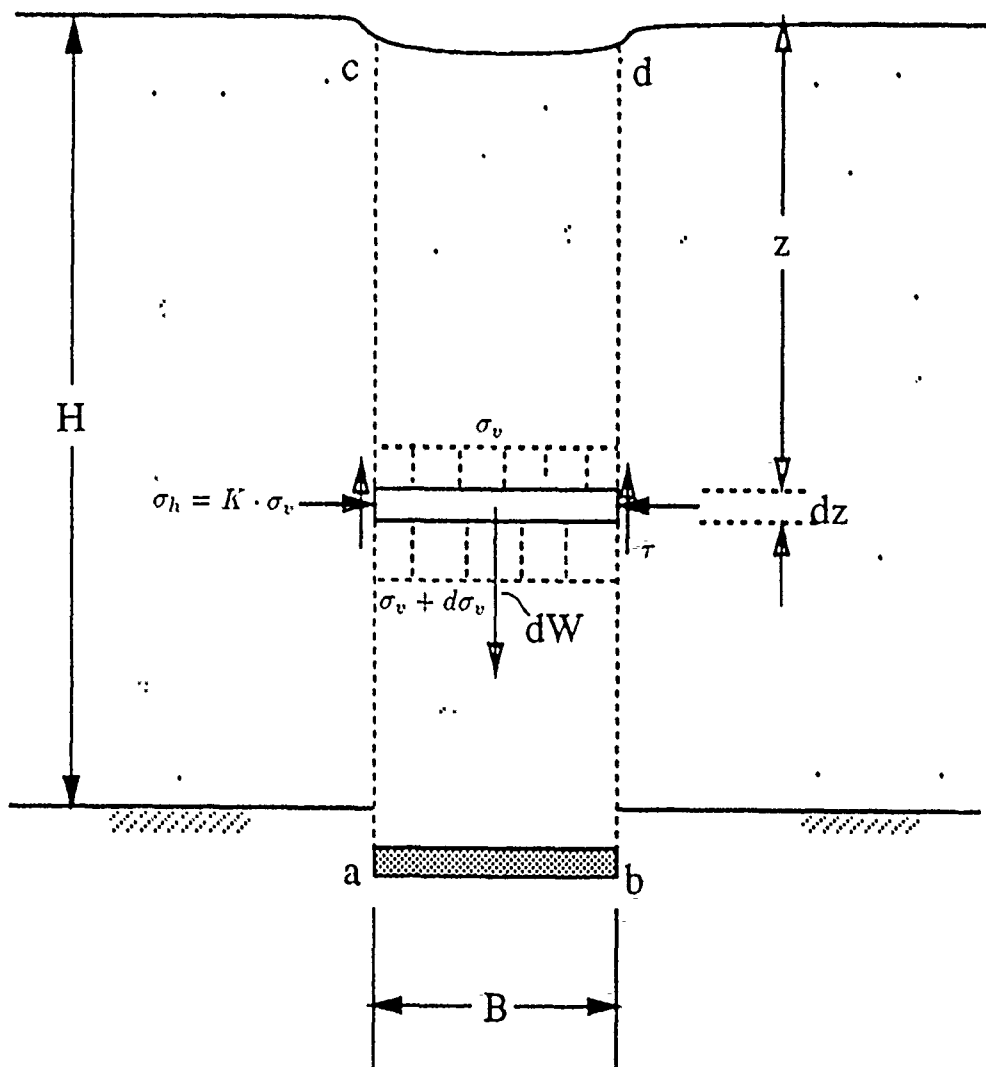


Figure 3.16: Deformation Pattern at Large Displacements

Consequently, we formulated a theory by combining the formulations of Engesser (1881), Bierbaumer (1913) and Evans (1983). The proposed expression for the minimum load is

$$P_{\min} = \gamma B^2 \left( \frac{K'}{2 \cot \phi + \frac{B}{H} K'} + \frac{\cot \phi}{6} \right) \quad (3.1)$$

where B is the width of the trapdoor, H is the depth of overburden,  $\gamma$  is the unit weight of the soil,  $\phi$  is the friction angle, and

$$K' = \frac{\cos^2 \phi}{1 + \sin^2 \phi}$$

The beauty of this new theory lies in the fact that one need not assume a value for the lateral coefficient of pressure K - the main source of controversy in the other methods. It comes about automatically from a Mohr circle construction by hypothesizing that the arch itself is a failure surface, with a slope from the vertical through the edges of the trapdoor equal to the friction angle of the soil. The shape of the arch is assumed to be a parabola, and the force on the trapdoor is the sum of the weight of material below this arch (which depends on B,  $\gamma$  and  $\phi$ ) and the effect of the induced stresses from the sides due to the load redistribution (which is a function of H,  $\gamma$  and  $\phi$ ).

Computations in this study have shown that the predicted minimum load on the structure (trapdoor) is approximately the same whether the shape of the arch is curved, as in Engesser's theory, or triangular, as in Bierbaumer's or Evan's theory. Both shapes have indeed been observed experimentally, with the triangle-like pattern occurring at larger displacements. Thus, even if the arch configuration transforms from a curved to a triangular shape while the door is moved down, the load on the door is apparently unchanged. This may explain why the measured forces, as soon as the minimum is reached, stay at more or less the same level for a considerable amount of displacement.

The trapdoor experiments both with granular and jointed media have shown some interesting similarities. Specifically, the formation of a physical arch in the former is analogous to the brick stack case. As observed by Stone (1988) in his centrifuge tests, the rupture surfaces tend to become vertical as the trapdoor is continually lowered - just like in the direct stack arrangement.

### 3.6 Concluding Comments and Outline

The three objectives of this research, to study arching in granular and jointed media in the realistic geostatic stress environment of the centrifuge, to examine the applicability of centrifuge testing through a modelling the model approach and the development - if necessary - of a new arching theory were achieved. Arching leads to a load reduction as the trapdoor displaces. In previous arching experiments under normal gravity a minimum load was reached followed by a relatively rapid load increase afterwards while in the centrifuge at high g levels the load increased very slowly after the minimum. This can have a significant effect on tunnel design where one assumes a load reduction with displacement but, so far, has been very conservative as far as the admissible displacements are concerned. The reason for this conservatism is the possibility of loosening, i.e. the development of the higher ultimate load. As shown, this ultimate load develops very slowly under realistic stress conditions.

We were able to pretty conclusively determine that centrifuge testing is applicable in modelling with granular materials while the applicability is limited in jointed media. The fact that shearing resistance in discontinua depends on absolute and not relative displacements is the reason for this.

The trapdoor tests and a number pre-existing arching theories allowed us to develop a new arching theory which considers the fact that a real arch of parabolic or triangular shape occurs above the trapdoor. The load is independent of the lateral stress coefficient (in contrast to other arching theories).

Future work will have to extend this arching theory to the ultimate load. In this context, physical experiments in the centrifuge will be needed to accurately establish the transformation of the arch into a prismatic body. In spite of the fact that the applicability of centrifuge testing to discontinua is limited, cases in which the geostatic stress conditions may be more important than displacement related phenomena need to be studied. Examples are rigid block/wedge concepts as used in slope stability analysis.

## 4. Stochastic and Topological Fracture Geometry Model

### 4.1 Problem Statement and Possible Approaches

Attempts at describing the geometric patterns of rock joints are numerous. During the past 10 to 15 years, much of this effort has been directed toward the development of stochastic models, and the MIT rock mechanics group has played a leading role. The basic concept of these models is to statistically sample geometric joint characteristics, such as orientation, trace length and spacing (location) followed by a probabilistic model representation of the sampled data. Ideally the modelled and real pattern should coincide (within the acceptable statistical range). Given the uncertainty of joint geometry (variability or range of characteristics; limited access through exploration) probabilistic or stochastic approaches represent in most cases the only possible way to come up with engineering solutions to flow, -stability, - and deformability problems. Many geological problems also rely on stochastic representation of geometry for their solution.

However, the existing models have to resort to significant simplifications, specifically:

- They (with some exceptions) do not account for spatial nonhomogeneities such as fracture clustering.
- The models are only loosely tied to the geologic genesis of the fractures. In particular, most models assume independence among fracture sets. From a physical viewpoint, this assumption is often incorrect.
- Only in a few cases have the models been validated using actual fracture data.

As a consequence, some modelled (simulated) joint patterns closely represent the real conditions while others do not. It is also desirable to model joint geometry in a way that corresponds to joint genesis. Individual joints and joint sets grow in a mechanically based sequence. The geometric model should be capable of producing joints and joint sets in such a sequence. Eventually, one will then be able to link the geometric and mechanical models to represent joint patterns at particular sites.

What we were trying to do in this research is to develop stochastic models which more realistically represent joint patterns than the existing ones, and which allow one to model the sequence of joint genesis. (Eventually, such geometric models will be combined with mechanical models such as those obtained from the research discussed in Section 2, above).

Figure 4.1 shows typical joint trace maps, i.e. the intersections of joints with the outcrop surface. There are three basic approaches to model joint patterns such as the ones shown in Fig. 4.1.

- Point-based processes. For instance the midpoint distribution of joint traces is modelled. It is then possible to have "marks" on each midpoint which describe the length (size), orientation and other characteristics of the particular joint.
- Fiber processes. The trace distribution is directly modelled but marks can again be added to characterize other properties such as size in the third dimension, and roughness.
- Random closed sets (RACS) model the joints as planar features (i.e. the distribution of planar features). Again, other properties such as nonplanarity can be associated with each feature.

These three approaches essentially go from the one dimensional to the three dimensional. If the basic approach is simple (one dimensional) other characteristics need to be associated through separate processes (The "marks" discussed above). So far we have looked into and, where appropriate developed, point and fiber processes.

In our investigation of point processes, we tested the 1) homogeneous, isotropic Poisson point process. 2) inhomogeneous Poisson point process; 3) Poisson cluster process; 4) Cox (doubly stochastic) process; 5) simple inhibition process; 6) thinning process; 7) soft core process.

In figure 4.2 the midpoints of the joint traces within the rectangular area of Fig. 4.1a are shown. Tests of complete spatial randomness based on interevent distances and nearest neighbor distances as well as second moment properties indicate that the points in Fig. 4.2 do not follow a homogeneous Poisson process. The

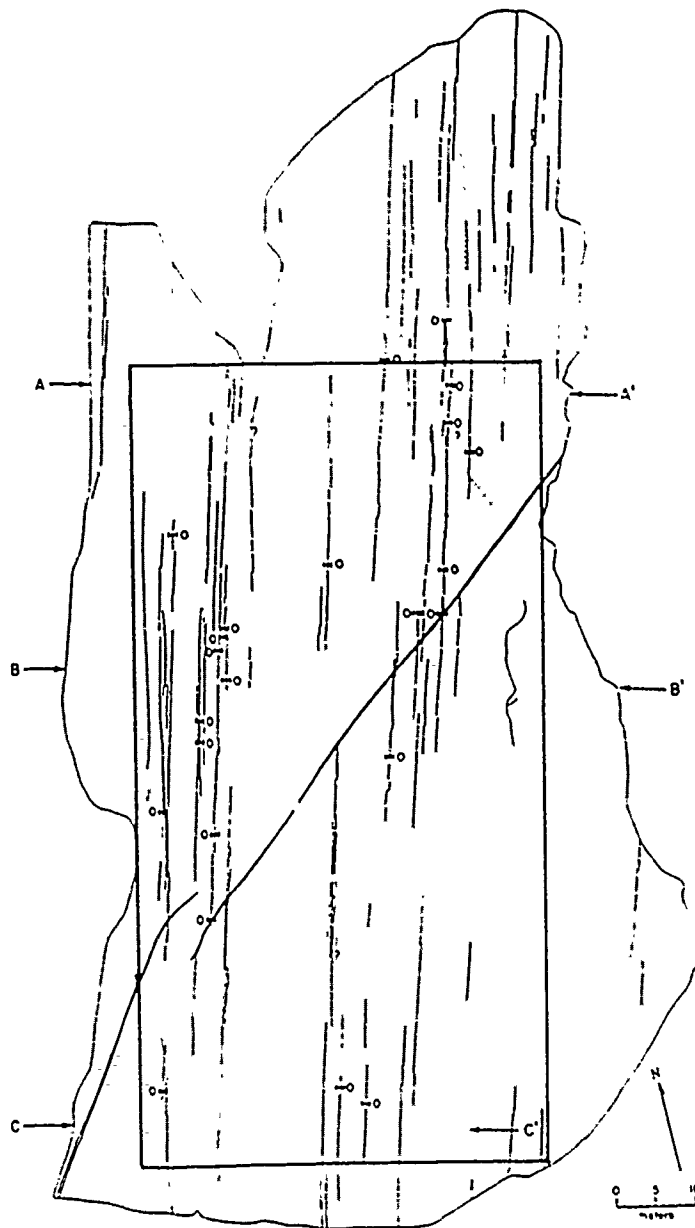


Figure 4.1a. Map of Florence Lake Outcrop (After Segall and Pollard, 1983; Only Traces Within Rectangular Region are Considered)

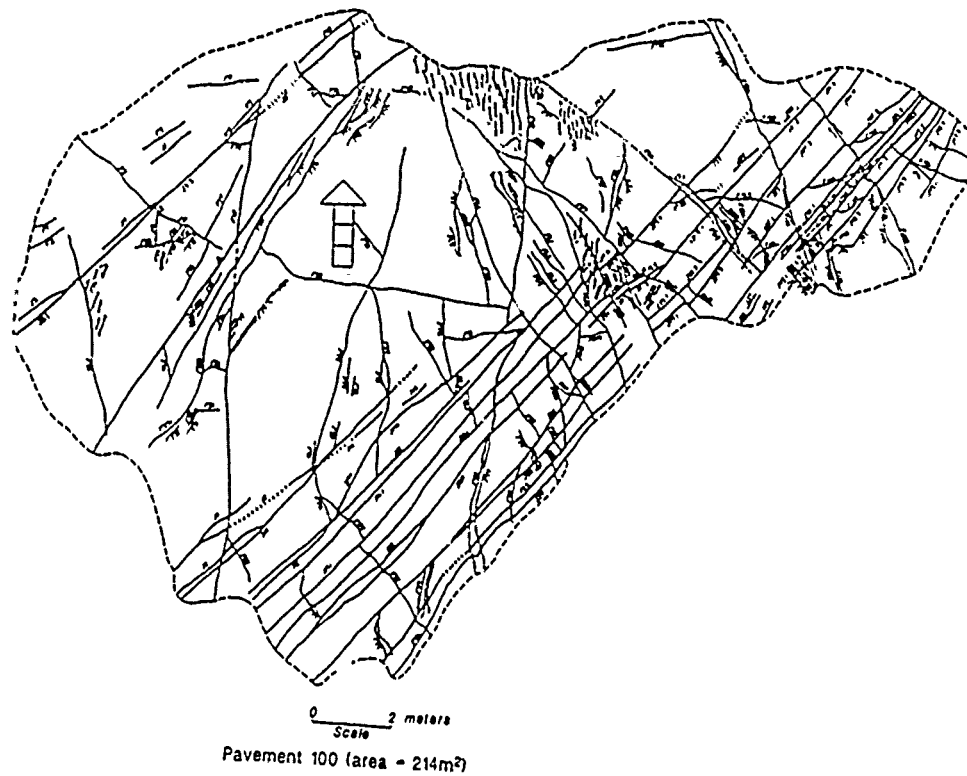


Figure 4.1b. Trace Map of PA100 (From Barton and Larson, 1985).

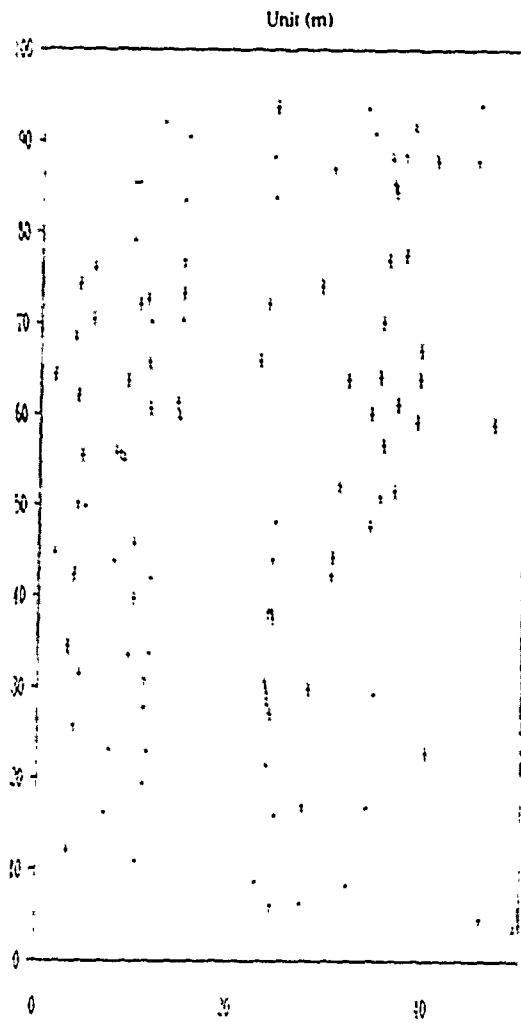


Figure 4.2. Mid Point Representation of Traces of Florence Lake Outcrop.

Inhomogeneous Poisson Point Model and the Doubly Stochastic (Cox) Model were applied. With the inhomogeneous Poisson Point Model we also included the joint trace length as a mark on each point. Nevertheless, this model requires that joint intensity variations be estimated with kernel functions. These kernel functions are not explicit and make thus estimation of joint patterns outside the narrow observed area difficult. This problem does not exist with the doubly stochastic process, where the intensity function is an explicit stochastic function. Fig. 4.3 shows the midpoints produced with the Cox process which produces a pattern very similar to that shown in Fig. 4.2. The statistics, such as the second moment analysis, confirm this.

In the area of fiber or line process models we also investigated a number of possibilities such as the homogeneous Poisson fiber process, the parent daughter model, the fractal model, the branching model, the hierarchical model, the percolation model and the crack tessellation model.

## 4.2 Hierarchical Fracture Trace Model

### 4.2.1 Basic Concept

On the basis of our research into point and fiber processes, we then developed a hierarchical fracture trace model which allows one to realistically model several sets of fracture traces i.e. the intersections of fractures with an outcrop. So far, we have developed the model to handle two fracture trace sets, but an expansion to additional sets will be relatively simple.

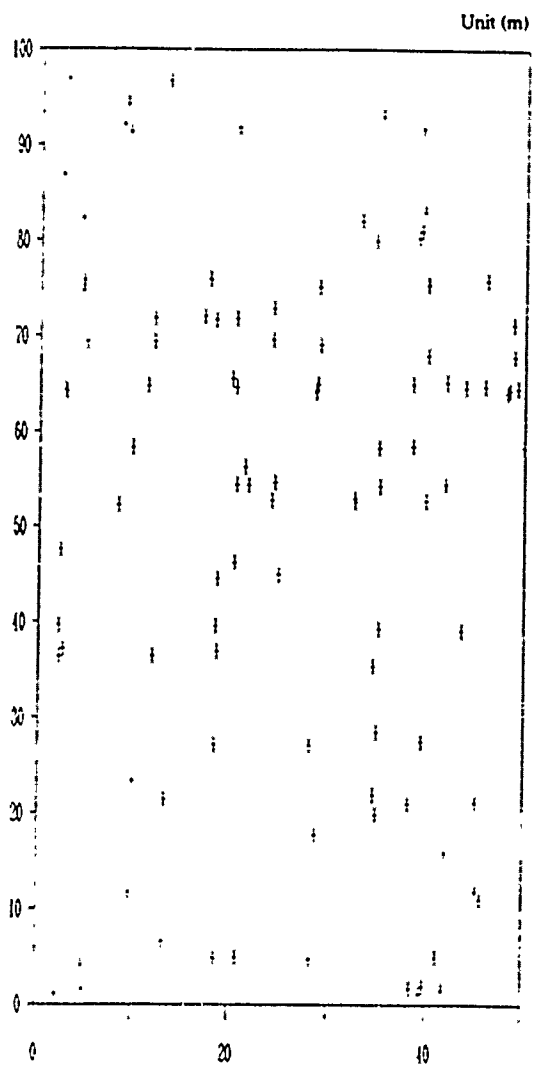


Figure 4.3. Mid Point Pattern Using Cox Process for Fracture Traces Shown in Figure 4.2.

The hierarchical modelling strategy consists of the following steps:

1. Model the midpoints of the first fracture set by a doubly stochastic (Cox) process, which allows one to represent spatial clustering.
2. Model the fracture trace length and orientation of the first set, including spatial correlation, if needed.
3. Test for dependence between the location (midpoints) of the second fracture set and the traces of the first set. If there is dependence, account for it when modelling the location of the second set; otherwise, model the second set independently, according to steps 1 and 2.
4. Model trace length and orientation of Set 2. Determine the probability of terminations at intersections of Set 2 fractures with Set 1 fractures and model the terminations.
5. Repeat for subsequent fracture sets (In the detailed development and example application included in this paper, only two sets will be considered).

Steps 3, 4 and 5 reflect the hierarchical aspect of the model.

The example used for illustration is pavement PA100 at Yucca Mountain (Fig. 4.1b) . A straight-segment idealization of the trace pattern is shown in Fig. 4.4. Two characteristic sets can be distinguished; Set 1 includes the joints with nearly parallel orientations and very few intersections. Set 2 collects the remaining traces, except for the intensely fractured zones. The decomposition into trace sets and the resulting patterns of midpoints are shown in Fig. 4.5.

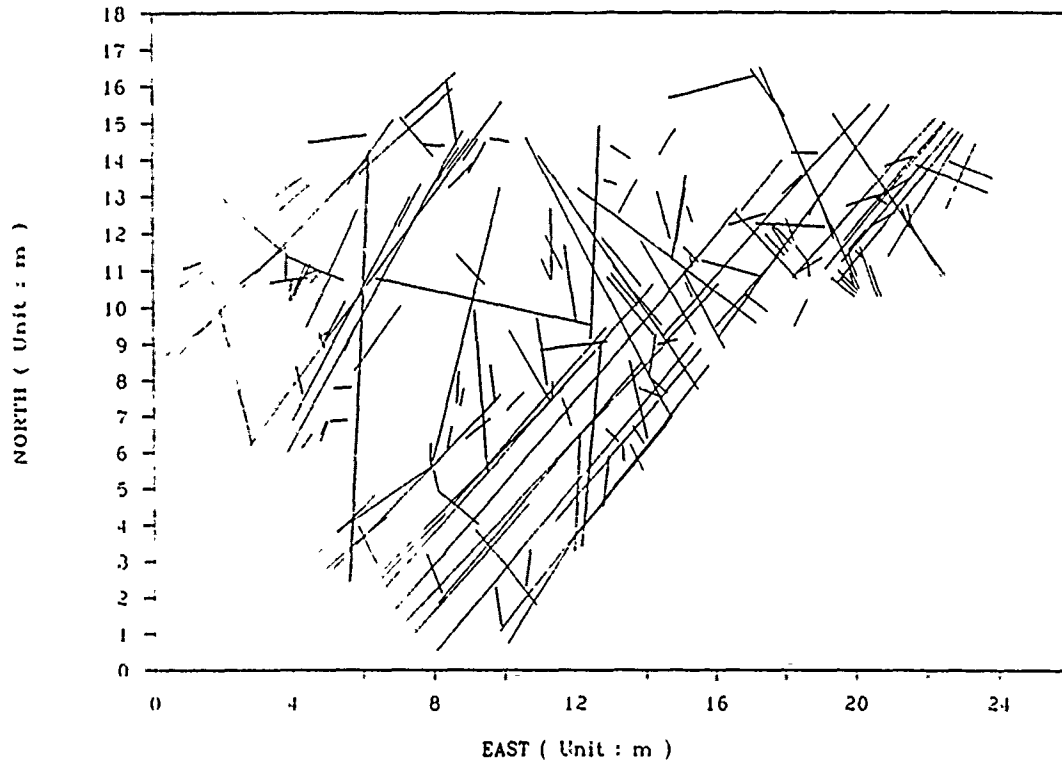


Figure 4.4. Digitized Trace Map of PA100.

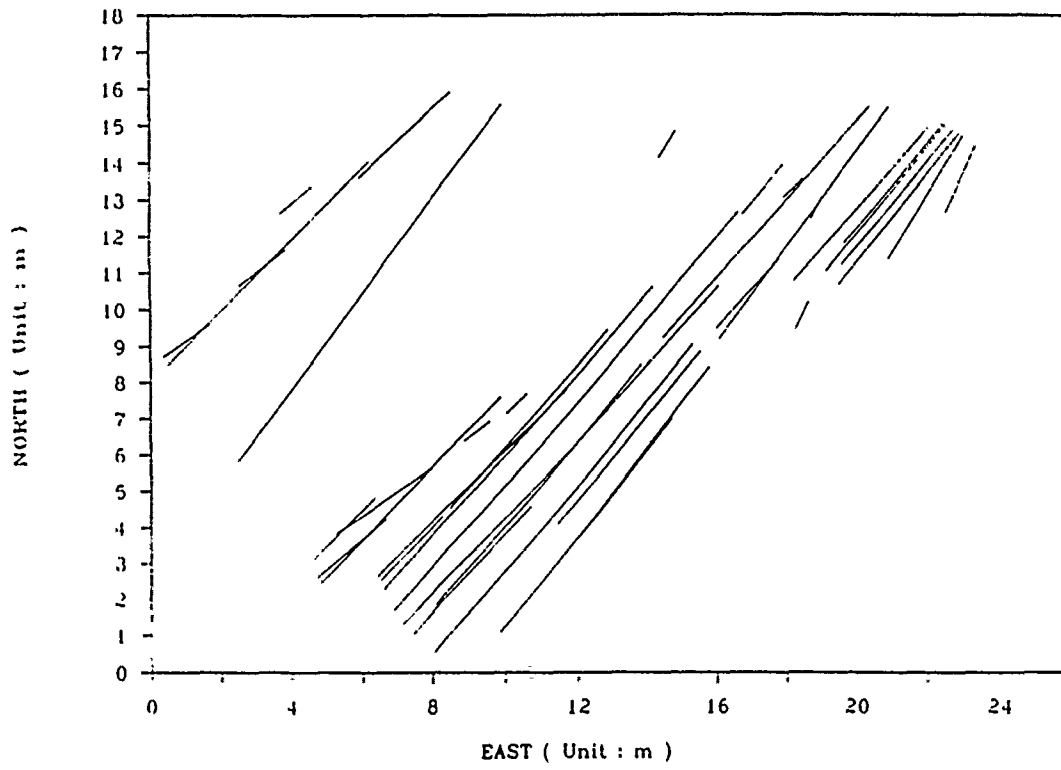


Figure 4.5a.. Digitized Trace Map of Set 1 (PA100)

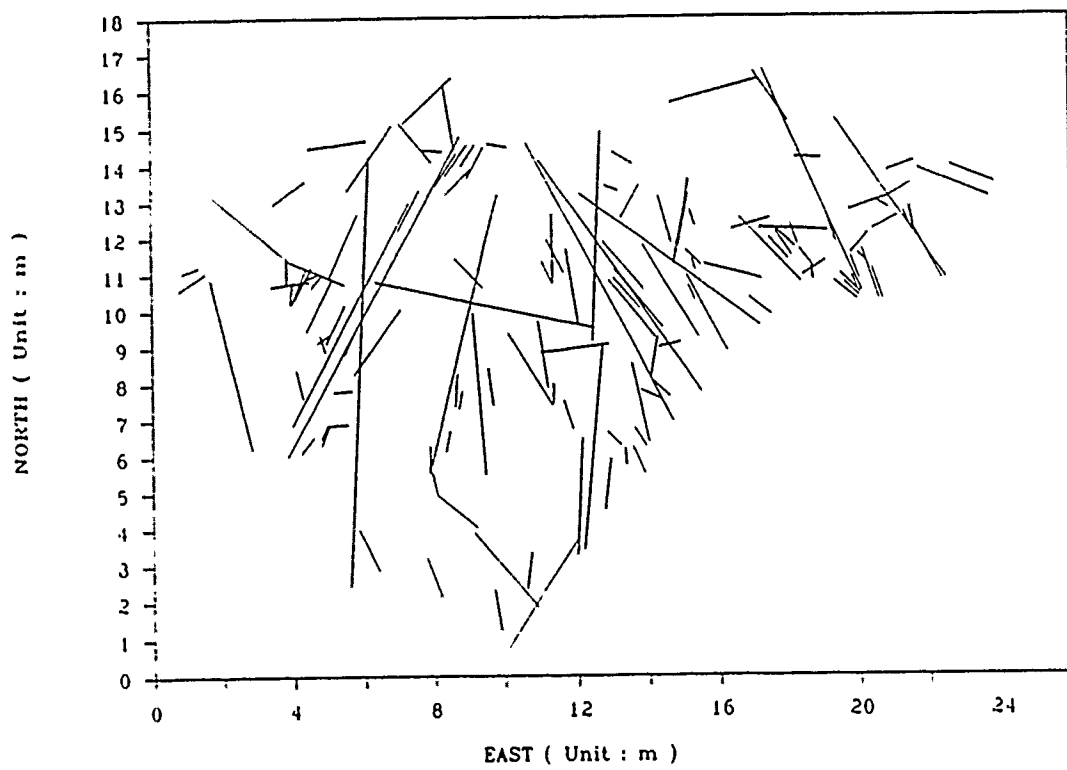


Figure 4.5b. Digitized Trace Map of Set 2 (PA100).

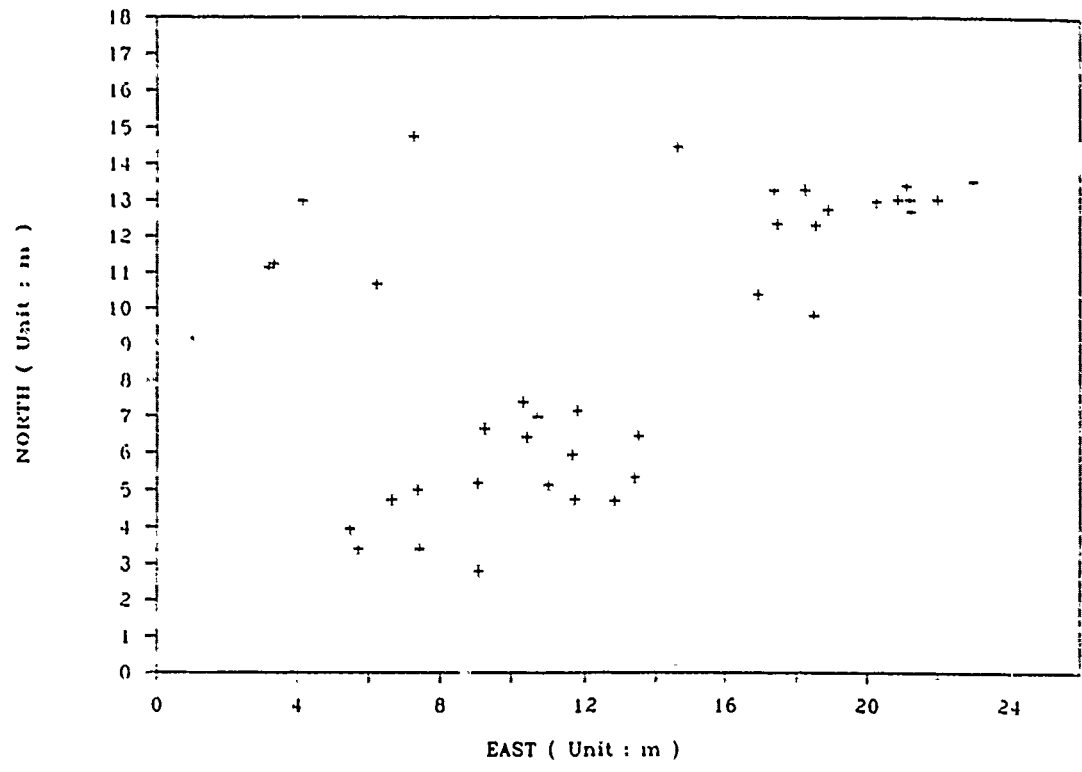


Figure 4.5c. Mid Point Map of PA100: Mid Points of Set 1 Traces Only.

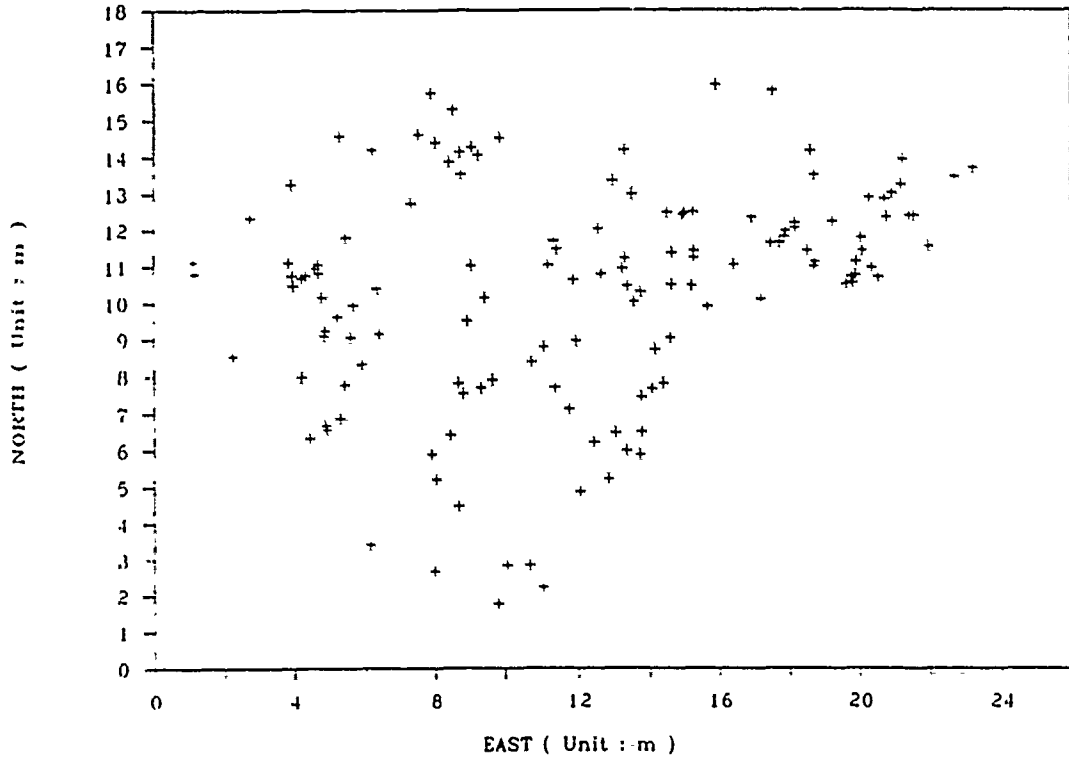


Figure 4.5d. Mid Point Map of PA100: Mid Points of Set 2 Traces Only.

#### 4.2.2. Modelling of the First Trace Set

As mentioned before, we have selected a Cox point process which was fitted to reproduce second-moment properties of the sample. More specifically we have aimed at matching the sample value of the function  $K_{ij}(t)$ . The indices  $i$  and  $j$  denote in general two sets of points, which for  $K_{11}$  coincide with the midpoints of Set 1 traces. For an unbounded region and a homogeneous Poisson process with index  $i$ ,  $K_{ii}(t) = \pi t^2$ , and for any two independent joint processes  $i$  and  $j$ ,  $K_{ij}(t) = \pi t^2$ . This is why the estimates  $K_{ii}(t) - \pi t^2$  and  $K_{ij}(t) - \pi t^2$  can be used to detect respectively deviations from Poisson homogeneity of a single point process and dependence between two point patterns. For regions with complex geometry, the expectations of  $K_{ii}(t) - \pi t^2$  and  $K_{ij}(t) - \pi t^2$  under the above conditions are not zero and are best obtained through Monte Carlo simulation. The Monte Carlo approach can be also used to devise acceptance regions at any specified significance level. For example, Figure 4.6 shows the mean value and the acceptance band (at significance level  $\alpha = 0.02$ ) of  $K_{11}(t) - \pi t^2$ , obtained through simulation of Set-1 midpoints using a specific Cox process. Superposed on the same figure is the empirical function  $K_{11}(t) - \pi t^2$ , obtained from the data in Figure 4.5c. The agreement is quite good over the entire range of distances at which clustering is present. For comparison with Figure 4.5c, Figure 4.7 shows a realization of the fitted Cox process inside the actual outcrop area.

Next, the distribution of trace length is considered. As is well known the empirical distribution of trace length for the scan line method, may be severely biased. Biases exist also in samples from outcrops such as that of Figure 4.1b. A general method to correct for these biases is to obtain distribution parameter estimates by the method of maximum likelihood.

For this purpose, one must classify outcrop traces into three types T and measure their observed length  $L'$  and "window of

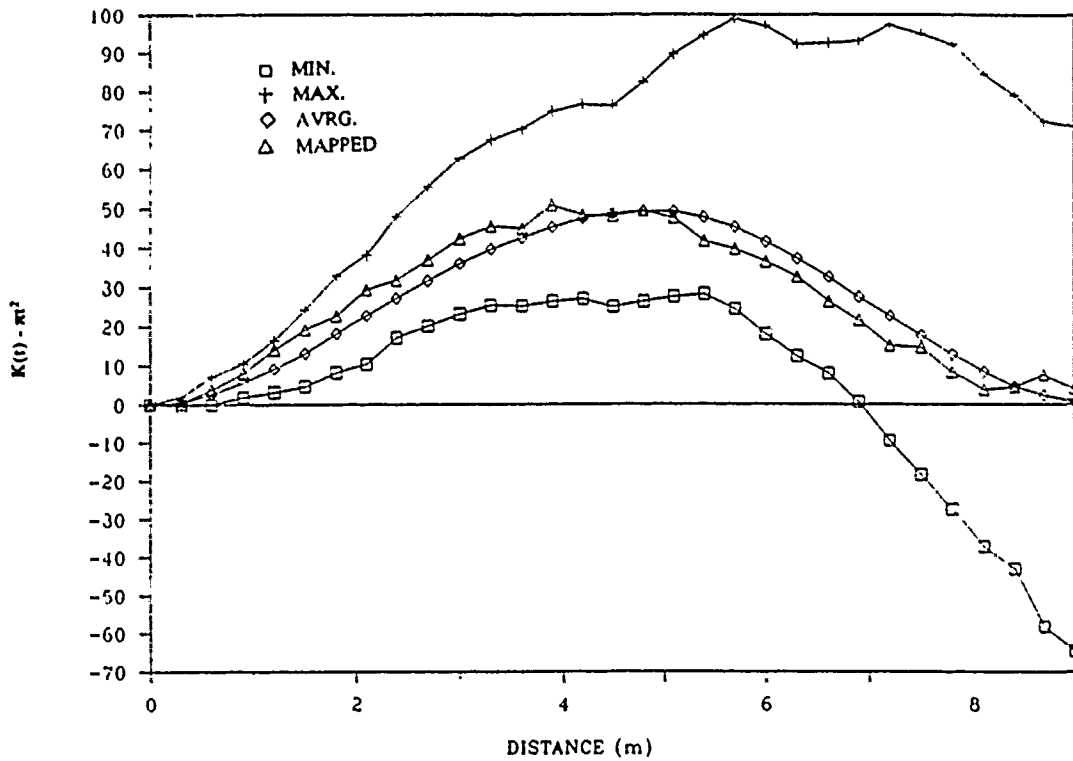


Figure 4.6. Second Moment Analysis of Set 1. Acceptance band (MIN to MAX) and average value (AVRG) obtained with model simulations are shown. The second moment of mapped data (MAPPED) is also given for comparison.

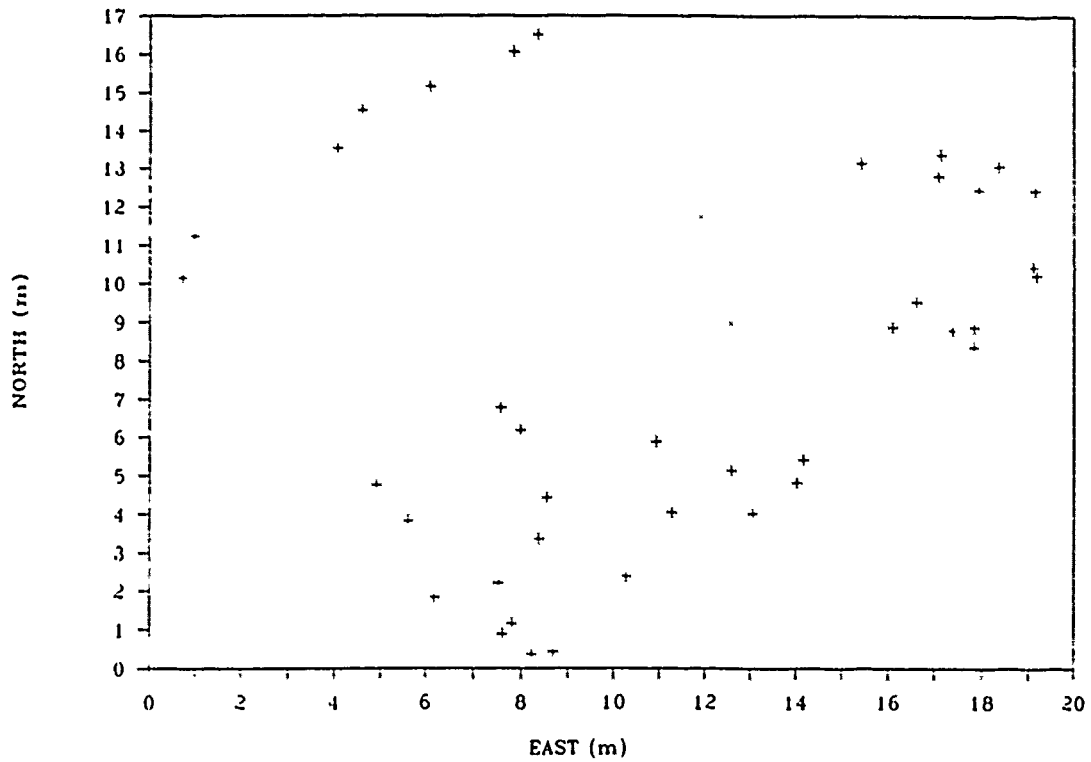


Figure 4.7. Simulation of Set 1 Mid Points with Cox Process.

observation"  $w$ , as illustrated in Figure 4.8. (Notice that, due to censoring, the actual length  $L$  of type 2 and type 3 traces exceeds the measured length  $L'$ ). The likelihood of the trace length distribution  $F_L$  can be expressed as a function of the sampled values  $T_i, w_i, L'_i$ , and the likelihood can be maximized to obtain estimates of the parameters. For example, Figure 4.9 shows the logarithm of lengths ' $l$ ' of Set 1 as a function of the mean trace length  $m$ , assuming that the Set 1 traces have exponential length distribution. The maximum likelihood estimate of  $m$  is about 7.0 m. It is interesting to notice that consideration of only Type 1 (fully exposed) traces would have given a much smaller estimate (2.75 m); see Figure 4.9.

For Set 1, we have not modeled the variability of trace orientation, since this variability is very modest. If it were important, orientation variability would be modelled analogously to what will be shown below for Set 2.

#### 4.2.3 Modelling of the Second Trace Set

Considerable complications may arise in the modelling of trace Set 2, due to dependence on the fractures of Set 1. One should start the modeling process by testing independence between the two sets of midpoints, for example, using the function  $K_{12}$  described above. When applied to the data in Figs. 4.5c and 4.5d, the test indicates significant interaction and more specifically a tendency of Set 2 points to be located near Set 1 points. From a physical point of view, it is, however, more meaningful to consider interaction between the location (here, the midpoints) of Set 2 and the traces (not just the midpoints) of Set 1. For this purpose, the point processes of midpoints of Set 2 were considered with intensity functions  $\lambda_2(x,y)$  which include the fact that the midpoint locations of Set 2 depend on the location of Set 1 traces.  $K_{12}$  can then be computed using such a (theoretical) intensity function. Figure 4.10a shows the match between the theoretical and empirical  $K_{12}$  functions. The fit is obviously good and the empirical function remains far from the bounds of the acceptance region at the 0.02 confidence level.

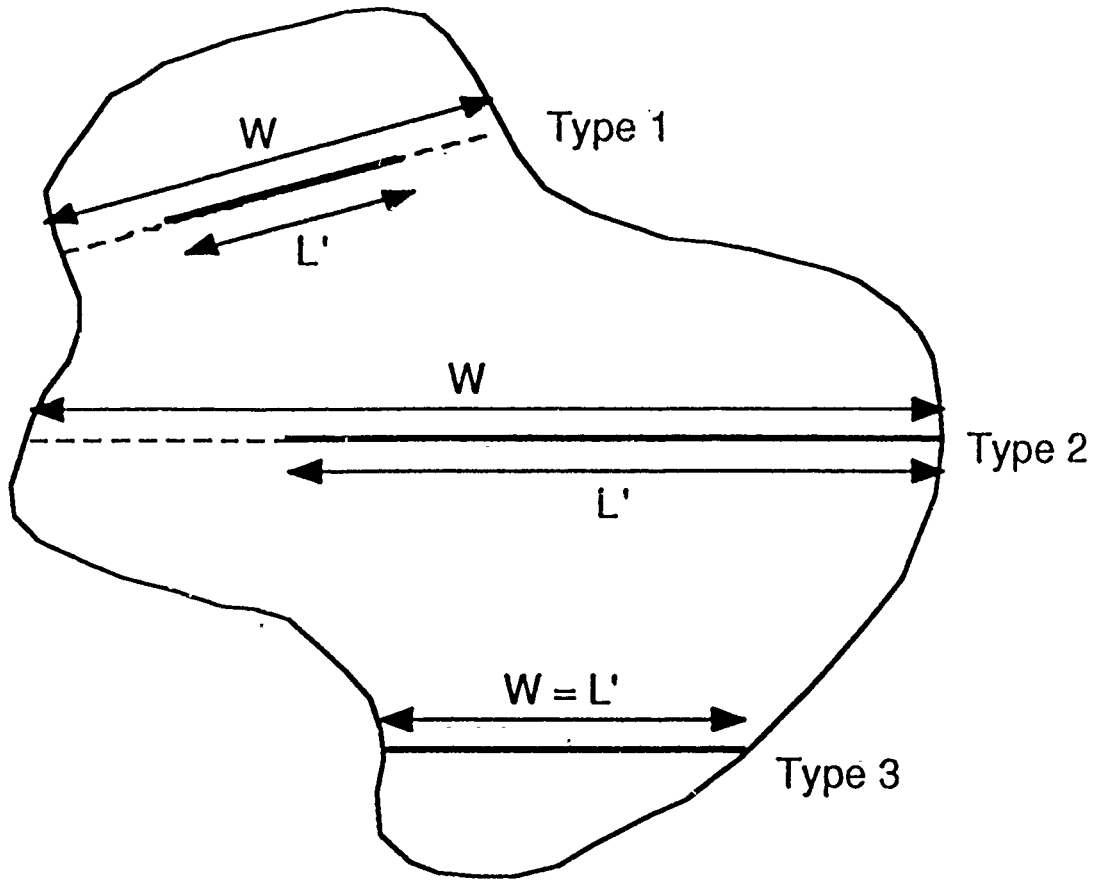


Figure 4.8. Notation for Maximum-Likelihood Estimation of Trace Length Distribution.

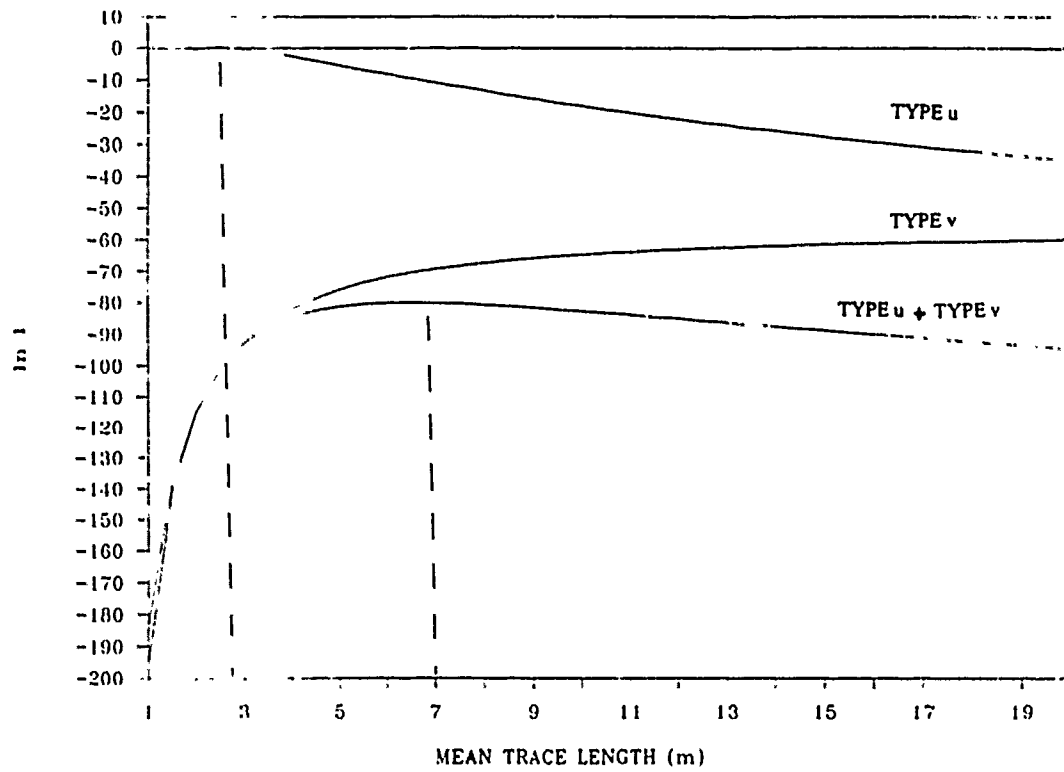


Figure 4.9. Log-Likelihood of Mean Trace Length for Set 1, Assuming Exponential Distribution.

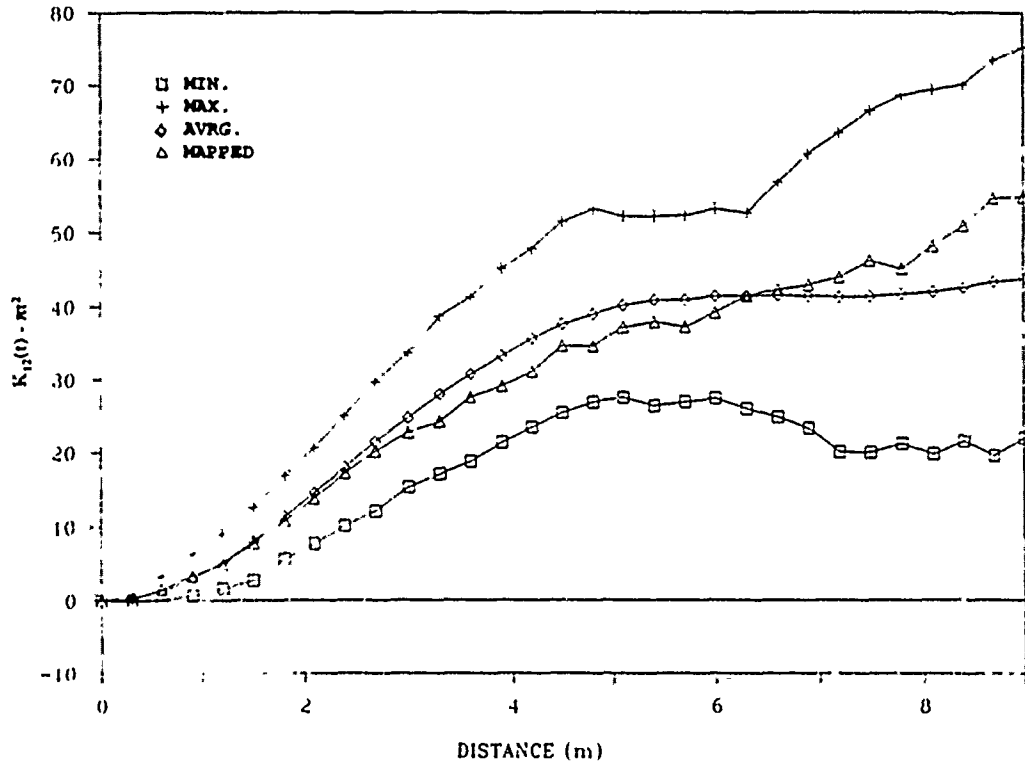


Figure 4.10a. Bivariate Second Moment Analysis for Sets 1 and 2 - Mid Point Correlation based on the Nearest Neighbor Function Method. Acceptance band (MIN to MAX) and Average Value (AVRG) are obtained with model simulations, while the mapped pattern (MAPPEI) is from actual data.

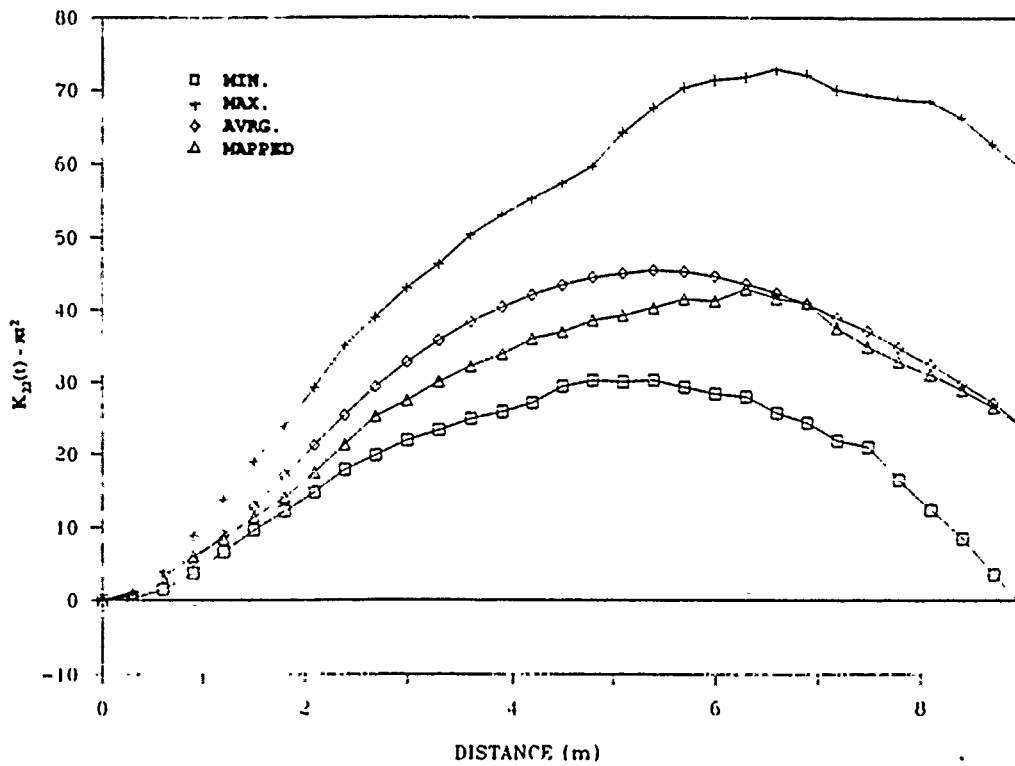


Figure 4.10b. (Univariate) Second Moment Analysis for Set 2 Mid Points Using the Nearest Neighbor Function Method Symbols are the same as those in Figure 4.10a.

However, the model still needs validation, because the  $\hat{K}_{12}$  function was used in the estimation of the function  $K$ . A specific concern is that the spatial variation of  $\lambda_2$  might not completely explain the clustered pattern of Set 2 points. A verification can be made by considering the function  $K_{22}(t)$ : this function is quite different from  $K_{12}$  and therefore is an appropriate choice for validation. A comparison of  $\hat{K}_{22}(t) - \pi t^2$  with results from simulating nonhomogeneous Poisson patterns with intensity  $\lambda_2$  is shown in Figure 4.10b, while Figure 4.11 reproduces a typical simulated pattern which should be compared to the real data in Fig. 4.5d. These results clearly confirm the model.

The estimation of the trace length distribution of the second set was done as for the first fracture set. The result is that such a distribution can be taken as exponential, with a mean value around 2 meters.

Orientation of Set 2 traces was modelled by fitting either a von Mises or a wrapped normal distribution.

Regarding termination of Set 2 traces on Set 1 traces, T-intersections, i.e. terminations and X-intersections, i.e. crossings are considered. The empirical probability of T and X intersections ( $P[X]=1-P[T]$ ) were determined. These probabilities have then been used as follows (Fig. 4.12):  $t_2$  is a generic simulated type-2 trace, and A and B are intersection points of  $t_2$  with type-1 traces closest to its endpoints (Fig. 4.12). For some type-2 traces, there may be only one A or B point, or none. The points A and B are converted to T-terminations, independently of each other and with probability  $P[T]$ . This procedure introduces some distortion in the distribution of trace-2 lengths; however, the resulting bias does not appear to be serious.

The final result of applying the hierarchical model is given in Fig. 4.13, where a simulation of Set 1 traces through the midpoints of Figure 4.7 and of Set 2 traces using the conditional model just described is shown. Not only has each step in this model been statistically tested, but the simulated pattern also appears to be close

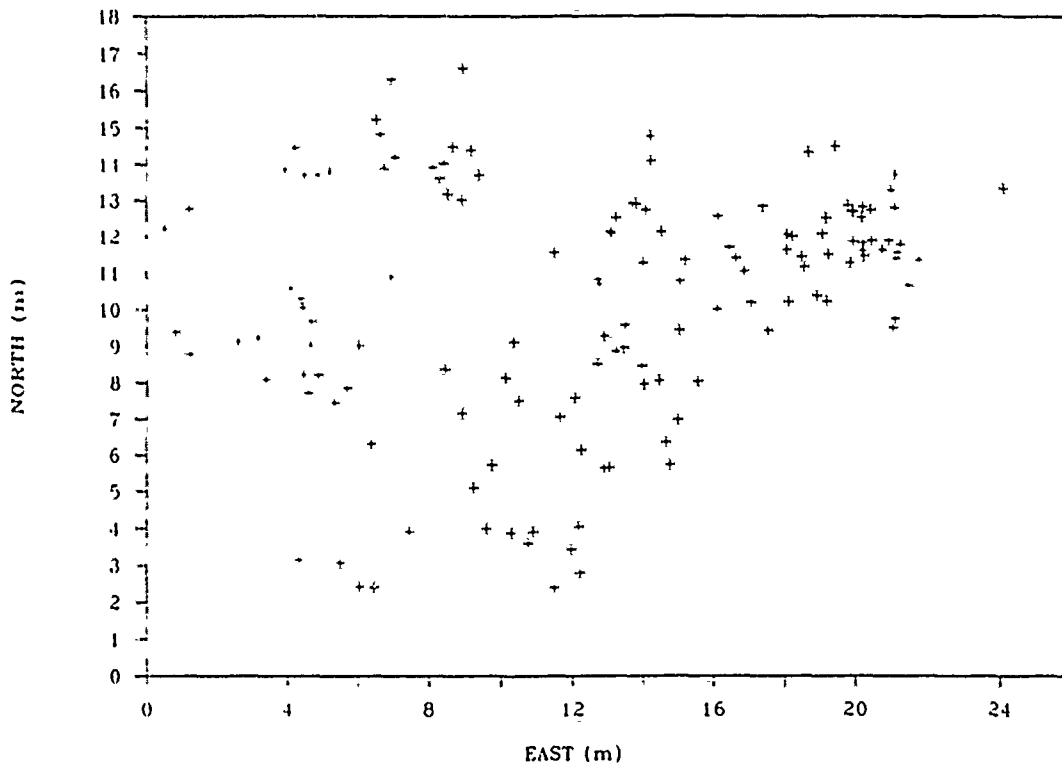


Figure 4.11. One of the Simulated Mid Point Patterns of Set 2 Using the Nearest Neighbor Function Method to Express Correlation.

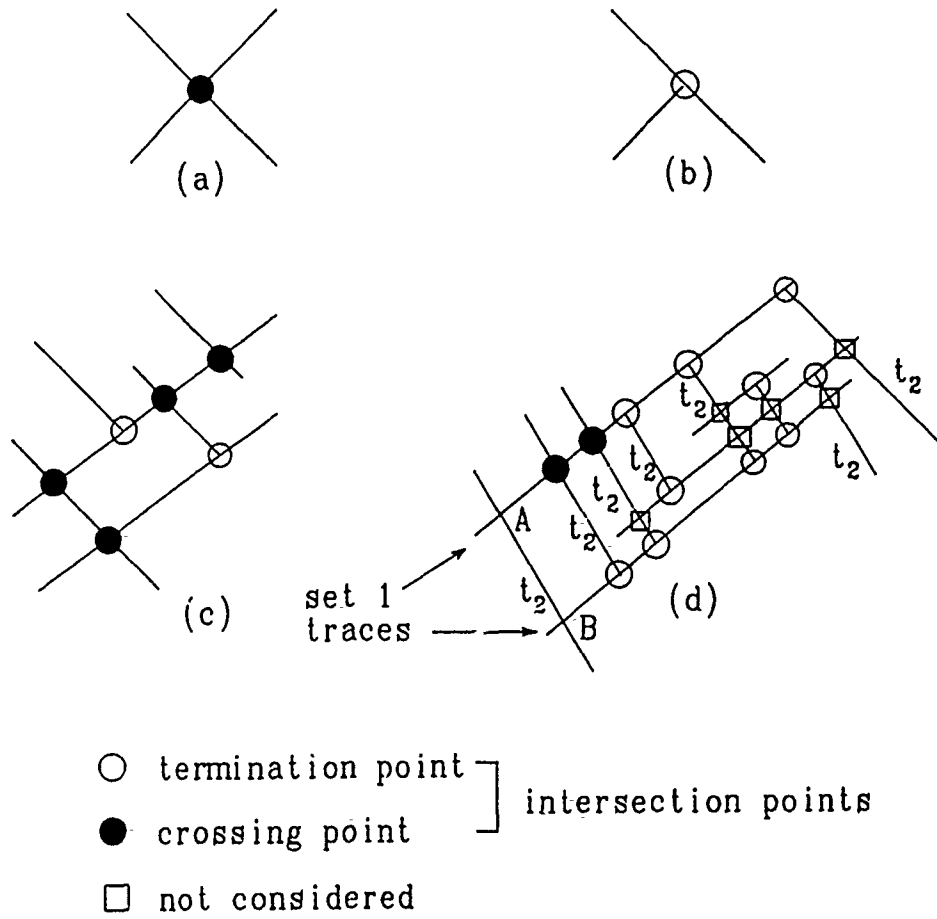


Figure 4.12. Calculation of Termination Probability.

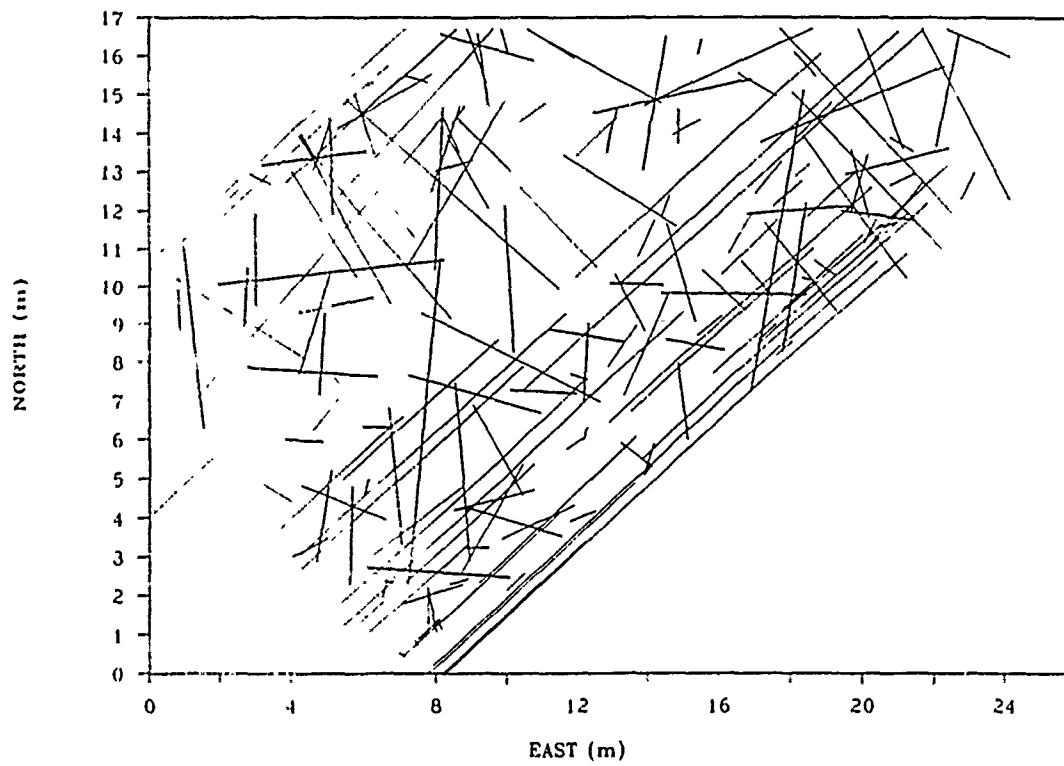


Figure 4.13. One of the Simulated Patterns of PA100 with the Von Mises Orientation Distribution Function.

to reality when one compares Fig. 4.13 with the original data in Fig. 4.1b.

### 4.3 Topological Model Applied to Slope Stability Analysis

#### 4.3.1 Principle

The hierarchical fracture geometry model was incorporated in a topological model for slope stability analysis. In its present state this model is two dimensional like the hierarchical fracture trace model, and it assumes fully persistent fractures. It is based on rigid body assumptions. In this approach slope stability is analyzed as follows:

1. Geometric construction of fracture paths: Depending on the actual fracture pattern, either the homogeneous Poisson point (or fiber) process model or the hierarchical fiber process model can be used to generate the network of fractures in a given two dimensional slope (the hierarchical fracture model is at present limited to two dimensions).
2. Kinematic analysis: All geometrically possible rock blocks (i.e., fully persistent blocks) that can be produced with the fracture pattern are simulated and those which are kinematically admissible are identified.
3. Kinetic (or mechanical) analysis: Using an appropriate mechanical model, the kinetic stability of the kinematically admissible blocks is determined.

#### 4.3.2 Fracture Patterns

The fracture network is created using the hierarchical fracture geometry model. Once the slope boundaries and fracture network are generated, one needs to find the effective fractures. An "effective fracture" is defined as a fracture which can be a part (i.e., a face) of a rock block. It must, therefore, have at least two intersection points with other fractures or with the slope boundaries.

In essence, effective fractures are inter-connected fractures. Effective fractures are thus relevant both in slope stability problems and in flow through rock masses. The elimination of the non-effective fractures which is done through sequential iteration is also important with regard to the computer program storage design since the effective fractures rather than total number of fractures or intersection points are used to define kinematically admissible fracture paths. As a consequence, one can improve the efficiency of the path-searching algorithm.

A so called connectivity matrix is constructed to find all fracture paths which delineate fully persistent rock blocks. Fig. 4.14 shows the connectivity matrix and the searching scheme to find the fracture paths. One essentially starts from the slope face and proceeds from intersection point to intersection point to determine the fracture paths. These paths have to either connect the face to the top surface or back to the face.

#### 4.3.3 Kinematic Analysis

After constructing the connectivity matrix, all fracture paths are checked to eliminate kinematically is admissible paths.

Inadmissible paths are (see also Figs. 4.15):

- The relative location of the subsequent intersection point on a path lies in region IV.
- Parts of the rock block are convex or concave as shown in Fig. 4.15b. This fact is recognized in the search routine with the connectivity matrix if a particular row in the connectivity matrix is encountered again.
- Face to face paths in which the location of the starting intersection point is higher than the end point (Fig. 4.15c), even if otherwise kinematically admissible. This prevents double counting of paths.
- Tapered paths (Fig. 4.15d). Subsequent values of inclination angles of path segments pointing toward the face are greater than the inclination angle of the fracture on which the block slides.

In essence, effective fractures are inter-connected fractures. Effective fractures are thus relevant both in slope stability problems and in flow through rock masses. The elimination of the non-effective fractures which is done through sequential iteration is also important with regard to the computer program storage design since the effective fractures rather than total number of fractures or intersection points are used to define kinematically admissible fracture paths. As a consequence, one can improve the efficiency of the path-searching algorithm.

A so called connectivity matrix is constructed to find all fracture paths which delineate fully persistent rock blocks. Fig. 4.14 shows the connectivity matrix and the searching scheme to find the fracture paths. One essentially starts from the slope face and proceeds from intersection point to intersection point to determine the fracture paths. These paths have to either connect the face to the top surface or back to the face.

#### 4.3.3 Kinematic Analysis

After constructing the connectivity matrix, all fracture paths are checked to eliminate kinematically inadmissible paths.

Inadmissible paths are (see also Figs. 4.15):

- The relative location of the subsequent intersection point on a path lies in region IV.
- Parts of the rock block are convex or concave as shown in Fig. 4.15b. This fact is recognized in the search routine with the connectivity matrix if a particular row in the connectivity matrix is encountered again.
- Face to face paths in which the location of the starting intersection point is higher than the end point (Fig. 4.15c), even if otherwise kinematically admissible. This prevents double counting of paths.
- Tapered paths (Fig. 4.15d). Subsequent values of inclination angles of path segments pointing toward the face are greater than the inclination angle of the fracture on which the block slides.

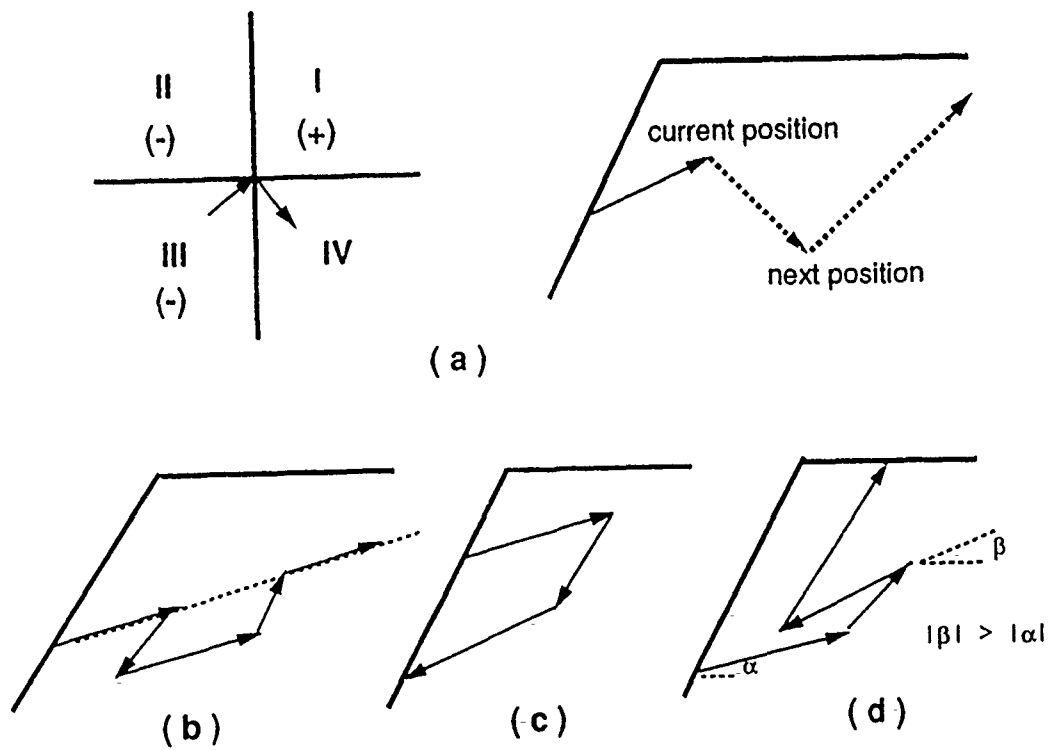


Figure 4.15. Kinematically Inadmissible Fracture Paths.

The assumption that slope failure occurs only through movement of intact blocks and not by fracturing of the intact material implies that only sliding along fractures or separation of fracture surfaces are possible. Sliding can kinematically only take place along the fracture with the smallest dip angle. This fracture will be identified in the kinematic analysis and so will be the ones which separate.

#### 4.3.4 Kinetic Analysis

As indicated before, the kinetic analysis is based on rigid body assumptions. Also, only sliding or separation along fractures is allowed but not toppling and no fracturing of intact material. The kinetic analysis is thus a limit equilibrium analysis with the sliding resistance represented by the Coulomb criterion, i.e. a friction angle and a cohesion, and the assumption of a so called "tensile cutoff stress" along fractures which separate. The tensile cutoff stress allows one to associate a tensile resistance to fracture separation. This actually represents an extension of the fully persistent model in which such a resistance would usually be zero.

#### 4.3.5 Parametric Studies

Parametric studies were conducted with the topological slope stability model. The parameters and the ranges of parameter states considered in this study are listed in Table 4.1. The effect of varying these parameters showed that the number of kinematically admissible rock blocks was largely controlled by the number of effective fractures which intersect the slope face, and that the most significant parameters in these slope stability analyses were the cohesion and friction angle which controlled the critical volume and thus the probability of failure. Orientation (mean and dispersion) had an effect also, while the tensile cut-off stress was not significant in the cases studied. Also interesting is the result presented in Fig. 4.16 which shows how strongly the assumed fracture geometry model affects the probability of fracturing.

Parameter	Fixed Value	Varied Range	Comments
Model			Homogeneous or Non-homogeneous Poisson Model
No. of Fracture Sets, $N_j$	1	2	
Cohesion, $C_j$	1000	0, 500, 1000, 1500	
Friction Angle, $\phi_j$	30°	10°, 20°, 30°, 40°	
Tensile Cut-off Stress, $\sigma_{oj}$	0	0, 10, 50, 100	
Orientation Concentration Factor, $\kappa$	20	10, 20, 30, 40	
Mean Fracture Orientation (Dip Angle), $\alpha$	40°	20°, 30°, 40°, 50°	
Mean Trace Length, $m_l$	6	4, 6, 8, 10	
Unit Weight of Rock Mass, $\gamma$	2200		Fixed

Table 4.1. Parameters Considered in Parametric Study  
Whenever a parameter is varied, all other parameters assume their fixed value.

#### 4.4 Concluding Comments and Outlook

The hierarchical fracture trace model produces fracture trace patterns which resemble reality very closely. It represents thus a marked improvement over the previously existing models. Most importantly, it is also capable of duplicating the sequential fracture genesis process which will usually occur in nature. This provides a sound basis for linking geometric and mechanical models of rock fractures and, very likely also for fractures in other materials. The topological slope stability model builds upon the stochastic fracture pattern model and provides a basis for more complex stability and deformation models of discontinua.

Future work in the stochastic modelling domain will have to consider more than two sets and the third dimension. The former is a relatively simple extension, the latter is a complex problem for which a number of approaches need to be investigated. Related to this problem is the consideration of other fracture characteristics such as deviation from a plane surface and varying mechanical properties. The topological model will have to be combined with more encompassing failure mechanisms. The fracture coalescence model developed in this research and described in Section 2 of this Executive Summary (as well as in Part I of the report series) is an obvious choice.

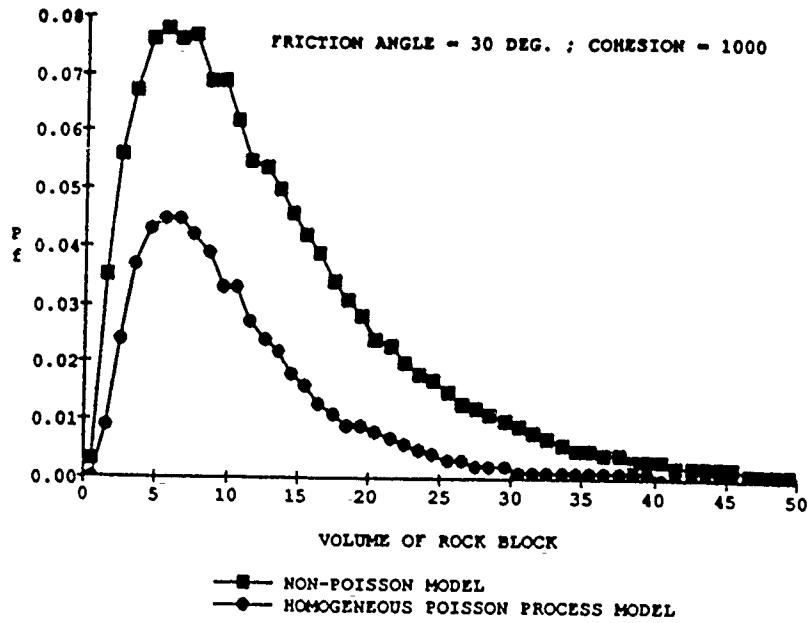


Figure 4.16.  $P_f$  Given Volume of Rock Block: Variation of Midpoint Model of Fractures.

## 5. Conclusions

The research on stochastic and centrifuge modelling of jointed rock resulted in significant contributions in the three major research areas.

In the area of "Fracturing of Fractured Rock" we found that pre-existing non-overlapping fractures coalesce through secondary cracks and not through wing cracks. A predictive model was developed and successfully validated. What has been discovered and developed in this context does potentially apply to any brittle discontinuum and may thus have far reaching implications.

In the area of centrifuge modelling, we found that arching in granular material under the realistic geostatic stress conditions involves large displacements during which the load remains near the minimum in contrast to previously known results which indicate a rapid load increase. An appropriate arching theory was developed. This research also showed that centrifuge modelling is applicable to granular materials with the usual scaling relationships while discontinua can be modelled only to a limited extent in the centrifuge.

In stochastic modelling of fractured rock we were able to develop a new hierarchical model which allowed us to accurately represent fracture trace patterns and, most importantly, their sequential genesis. The geometric fracture representation was incorporated in a topological model for slope stability analysis.

All these contributions are not only significant with regard to the advance in the state of the science but also regarding their practical implications. They also show very clearly in which way one should proceed to produce further specific and generally valid results.

## 6. Acknowledgements

The research results reflect the active interest and many technical discussions with the Technical Monitors, Dr. S. Wu of the U.S. Air Force Office of Scientific Research and Lt. S. Kuennen of the U.S. Air Force Engineering Sciences Center. Without them we could not have achieved what we did and this we would like to gratefully acknowledge.

## APPENDIX A

## Literature References

ABAQUS User's Manual, 1990. Hibbitt, Karlsson and Sorensen, Inc.

Barton, C.C.; Larson, E. 1985. "Fractal Geometry of Two-dimensional Fracture Networks at Yucca Mountain, Southwest Nevada, Proc. of Int. Symp. on Fundamentals of Rock Joints, 77-84.

Bierbaumer, A. 1913. "Die Dimensionierung des Tunnelmauerwerks", Engelmann, Leipzig.

Engesser, Fr. 1882. "Ueber den Erddruck gegen innere Stützwände (Tunnelwände)", Deutsche Bauzeitung, No. 16, pp. 91-93.

Evans, C.H. 1983. "An Examination of Arching in Granular Soils", S.M. Thesis, Dept. of Civil Eng., MIT.

Iglesia, G.; Einstein, H.H.; Whitman, R.V.; Jessberger, H.L.; Güttler, U. 1991. "Trapdoor Experiments with Simulated Jointed Rock", Centrifuge 91, Univ. of Colorado, Boulder.

Joseph, P. G.; Einstein, H.H.; Whitman, R.V. 1987. "A Literature Review of Geotechnical Centrifuge Modeling with Particular Emphasis on Rock Mechanics," MIT Report to the Air Force Engineering and Services Center, Tyndall Air Force Base, Florida.

Joseph, P.G.; Einstein, H.H., 1987. "Rock Modelling Using the Centrifuge", MIT Report to the Air Force Engineering and Services Center, Tyndall Air Force Base, Florida.

Lemaitre, J., 1986. "Local approach of fracture", Engineering Fracture Mechanics, 25, 5/6, pp. 523-537.

Reyes, O. M. 1988. "Numerical Modelling of Fracture Propagation in Tension Softening Materials", S.M. Thesis, Dept. of Civil Eng., MIT.

Rots, J.G.; Nauta, P.; Kusters, G.; Blaauwendraad, J. 1985. "Smearred crack approach and fracture localization in concrete", HERON, 30, 1.

Segall, P. ; Pollard, D.D. 1983. "Joint Formation in Granitic Rock of the Sierra Nevada", Geol. Soc. Am. Bull. 94:563-575.

Stone, K.J.L.; Güttler, U. 1989. "Bochum-MIT Collaboration on active arching experiments: Report from preliminary centrifuge tests", Ruhr-University Bochum.

Terzaghi, K. 1936. "Stress Distribution in Dry and in Saturated Sand Above a Yielding Trap-Door", Proc., First Int. Conf. on Soil Mech. and Foundation Eng., pp. 307-311.